

**PERIDYNAMIC BEAMS, PLATES, AND SHELLS:
A NONORDINARY, STATE-BASED MODEL**

APPROVED BY SUPERVISING COMMITTEE:

John T. Foster, Ph.D., Chair

Yusheng Feng, Ph.D.

Walter Richardson, Ph.D.

James Walker, Ph.D.

Xiaowei Zeng, Ph.D.

Accepted: _____
Dean, Graduate School

Copyright 2014 James O'Grady
All rights reserved.

DEDICATION

I would like to dedicate this dissertation to the memory of Thomas John O'Grady II, a passionate father and a passionate engineer

**PERIDYNAMIC BEAMS, PLATES, AND SHELLS:
A NONORDINARY, STATE-BASED MODEL**

by

JAMES O'GRADY, M.S.M.E.

DISSERTATION
Presented to the Graduate Faculty of
The University of Texas at San Antonio
In Partial Fulfillment
Of the Requirements
For the Degree of

DOCTOR OF PHILOSOPHY IN MECHANICAL ENGINEERING

THE UNIVERSITY OF TEXAS AT SAN ANTONIO
College of Engineering
Department of Mechanical Engineering
September 2014

ACKNOWLEDGEMENTS

This work was funded by grant number W911NF-11-1-0208 from the United States Air Force Office of Scientific Research.

I would like to thank my advisor, Dr. John Foster, for steering me onto a road I never knew existed and for pointing me at such an excellent problem.

Most of all, I would like to thank my wife, who has been endlessly supportive.

This Masters Thesis/Recital Document or Doctoral Dissertation was produced in accordance with guidelines which permit the inclusion as part of the Masters Thesis/Recital Document or Doctoral Dissertation the text of an original paper, or papers, submitted for publication. The Masters Thesis/Recital Document or Doctoral Dissertation must still conform to all other requirements explained in the Guide for the Preparation of a Masters Thesis/Recital Document or Doctoral Dissertation at The University of Texas at San Antonio. It must include a comprehensive abstract, a full introduction and literature review, and a final overall conclusion. Additional material (procedural and design data as well as descriptions of equipment) must be provided in sufficient detail to allow a clear and precise judgment to be made of the importance and originality of the research reported.

It is acceptable for this Masters Thesis/Recital Document or Doctoral Dissertation to include as chapters authentic copies of papers already published, provided these meet type size, margin, and legibility requirements. In such cases, connecting texts, which provide logical bridges between different manuscripts, are mandatory. Where the student is not the sole author of a manuscript, the student is required to make an explicit statement in the introductory material to that manuscript describing the students contribution to the work and acknowledging the contribution of the other author(s). The signatures of the Supervising Committee which precede all other material in the Masters Thesis/Recital Document or Doctoral Dissertation attest to the accuracy of this statement.

**PERIDYNAMIC BEAMS, PLATES, AND SHELLS:
A NONORDINARY, STATE-BASED MODEL**

James O'Grady, Ph.D.
The University of Texas at San Antonio, 2014

Supervising Professor: John T. Foster, Ph.D., Chair

Peridynamics is a nonlocal formulation of continuum mechanics in which forces are calculated as integral functions of displacement fields rather than spatial derivatives. The peridynamic model has major advantages over classical continuum mechanics when displacements are discontinuous, such as in the case of material failure. While multiple peridynamic material models capture the behavior of solid materials, not all structures are conveniently analyzed as solids. Finite Element Analysis often uses 1D and 2D elements to model thin features that would otherwise require a great number of 3D elements, but peridynamic thin features remain underdeveloped despite great interest in the engineering community. This work develops nonordinary state-based peridynamic models for the simulation of thin features. Beginning from an example nonordinary state-based model, lower dimensional peridynamic models of plates, beams, and shells are developed and validated against classical models. These peridynamic models are extended to incorporate brittle and plastic material failure, compounding the peridynamic advantages of discontinuity handling with the computational simplicity of reduced-dimension features. Once validated, these models will allow peridynamic modeling of complex structures such as aircraft skin that may experience damage from internal forces or external impacts.

TABLE OF CONTENTS

Acknowledgements	iv
Abstract	v
List of Tables	ix
List of Figures	x
Chapter 1: Introduction	1
1.1 Scope	1
1.2 Outline	2
Chapter 2: Literature Review	3
2.1 PDE-Based Failure Modeling	3
2.2 Peridynamic Modeling	8
2.3 Other Nonlocal Elasticity Models	12
2.4 Thin Features	14
2.4.1 Peridynamic Models	14
Chapter 3: Classical Background	18
3.1 Euler-Bernoulli Beam Theory	18
3.2 Kirchhoff-Love Plate Theory	21
Chapter 4: Peridynamics Background	21
4.1 Peridynamic States	21
4.2 State-based Models	22
4.3 Bond-based peridynamics	24
4.4 Important Peridynamic Models	26

4.4.1	Bond-based Elastic Solid	26
4.4.2	State-based Elastic Solid	29
4.4.3	Correspondence Models	30
Chapter 5: Model Development	32
5.1	Bond Pair Material Model	32
5.2	Bond Pair Beam in Bending	33
5.2.1	Energy Equivalence	33
5.2.2	Relation to Eringen Nonlocality	35
5.2.3	Weighting function and inelasticity	37
5.3	Bond Pair Plate in Bending	41
5.3.1	Energy Equivalence	41
5.3.2	Combining Bending and Extension Models	44
5.4	Extension to arbitrary Poisson ratio	46
Chapter 6: Numerical Simulation	49
6.1	Discretized Bond Pair Beam	49
6.2	Discretized Bond Pair Plate	50
6.2.1	Curved Shapes	51
6.2.2	Irregular Discretization	52
6.3	“Boundary” Conditions	54
6.4	Numerical Solution Method	56
6.5	Results	58
6.5.1	Straight Beam Results	58
6.5.2	Flat Plate Results	63
Chapter 7: Conclusion	69

Appendix A: Fréchet Derivative	71
A.1 Definition	71
A.2 Bond-Pair Force	71
A.3 Isotropic Bending Correction	72
Appendix B: Notations	74
B.1 Math Notations	74
Bibliography	75
Vita	

LIST OF TABLES

Table 3.1 Common Beam End Conditions	21
Table 4.1 Common State Operation Nomenclature	22

LIST OF FIGURES

Figure 2.1	XFEM includes discontinuous enrichment basis functions	4
Figure 2.2	XFEM models enrich nodes around a discontinuity	5
Figure 2.3	Comparison of domains of influence for FEM and RKPM	6
Figure 2.4	A peridynamic body Ω	9
Figure 2.5	Peridynamic model of an airplane impacting a concrete structure	10
Figure 2.6	Silling's illustration of coarse-graining in time	11
Figure 2.7	Tearing a peridynamic membrane	15
Figure 2.8	A peridynamic cylinder uses several nodes through its thickness	15
Figure 2.9	Taylor and Steigmann plate transverse displacement	16
Figure 2.10	Taylor and Steigmann plate cracking	17
Figure 3.1	Infinitesimal Beam Slice	19
Figure 3.2	Small deformation in an Euler beam	19
Figure 4.1	Deformation tensor vs. deformation vector state	21
Figure 4.2	The body Ω deformed by the deformation state \underline{Y}	23
Figure 4.3	Illustration of the three types of peridynamic models	24
Figure 4.4	Bond-based models can describe a variety of material behaviors	25
Figure 5.1	Illustration of a bond pair model that resists angular deformation	32
Figure 5.2	Deformation and force vector states	32
Figure 5.3	A continuous peridynamic beam with horizon δ	33
Figure 5.4	Euler beam moment contribution	38
Figure 5.5	Bond-pair moment contribution	38
Figure 5.6	Weight function for a beam of rectangular cross-section	39
Figure 5.7	Weight function for an I-beam	40

Figure 5.8	Illustration of a bond pair on a plate.	42
Figure 5.9	The Hybrid Model Combines Bending and Extension Components	45
Figure 5.10	Bending Deformation Decomposed into Isotropic and Deviatoric Portions	47
Figure 6.1	Discretized peridynamic plate with illustrated bond pair	50
Figure 6.2	Virtual Points Allow Straight Pairs on Curved Surfaces	52
Figure 6.3	Virtual Points Take the Displacement of Nearby Real Points	52
Figure 6.4	Virtual Points Pair Up Unpaired Neighbors	53
Figure 6.5	Barycentric interpolation is based on the relative areas of sub triangles	53
Figure 6.6	The boundary of a peridynamic model is a region of nonzero thickness	55
Figure 6.7	The uniform-load elastic beam is accurately modeled with few nodes	58
Figure 6.8	The clamped condition requires finer discretization	59
Figure 6.9	The clamped condition requires a smaller horizon	60
Figure 6.10	The elastic perfectly-plastic beam requires finer discretization	61
Figure 6.11	The need for fine discretization is even more apparent when representing residual plastic deformation	61
Figure 6.12	Accurately modeling residual plastic deformation also requires a small horizon	62
Figure 6.13	A brittle beam with prescribed center displacement	62
Figure 6.14	The Bond-Pair Model Converges on Accurate Plate Deflection with Smaller Horizons	63
Figure 6.15	Horizon Must Include Sufficient Nodes	64
Figure 6.16	The Bond-Pair Model Converges on Accurate Plate Deflection with Finer Discretization	65
Figure 6.17	The Combined Model Accurately Captures the Influence of In-Plane Tension	65
Figure 6.18	The Extended Model Matches for Arbitrary Poisson's Ratio	66
Figure 6.19	Crack Progression in Double Torsion Brittle Plate	67
Figure 6.20	Crack Progression in Single Torsion Brittle Plate	68

Chapter 1: INTRODUCTION

The final goal of many mechanical engineering analyses is the prediction and description of material failure. Even when some amount of material failure is acceptable, conservative engineering models can indicate safe conditions by which failure may be avoided. Within these operation envelopes, a wide variety of well-developed analysis techniques are available to predict material behavior. Outside the envelope, the onset of failure may be predicted and replacement/repair indicated, but the actual progression of material failure is unknown. Because these envelopes conservatively restrict operation, absolute avoidance of material failure may require tradeoffs such as: reduced operational life, expensive inspection and repair regimes, increased down-time, and reduced performance in other areas. Material models that accurately predict failure progression can extend the operational envelope without reducing reliability. Other problems, such as those related to impact, penetration, and blast resistance, necessarily involve material failure and cannot be accurately modeled without simulating failure progression. Without reliable means for modeling failure progression, these problems can be tackled only by means of extensive (and expensive) testing programs. While some extrapolation from test results is possible, many conditions of interest are difficult, expensive, and/or dangerous to create and to observe. For these reasons, accurate and reliable models for the progression of failure for various materials and conditions has long been and remains a major focus of engineering research.

1.1 Scope

This dissertation presents a peridynamic equivalent to an Euler-Bernoulli beam, along with a methodology for representing non-uniform cross-sections, plastic behavior, and failure. Unlike many continuum beam theories that derive new equations of motion (such as fourth order PDE's) from the 3D elastic constitutive model, the new model is not derived from prior ordinary peridynamic models based on bond extension, but is a material model that directly resists bending deformation while maintaining the same conservation of momentum equation as the 3D model.

This beam model is demonstrated to be equivalent to Eringen’s nonlocal elasticity for small peridynamic horizons. The 1D beam model is then extended to 2D to model the bending behavior of flat Kirchhoff-Love plates. The resulting 1-parameter model is constrained to a Poisson ratio $\nu = 1/3$. By introducing an *isotropic bending-state*, the model is extended to any valid Poisson ratio. The model is combined with an extension-based model to capture the effect of in-plane forces on bending behavior, resulting in a flat shell model. Introducing the concept of virtual points results in a model that is more practically applicable and able to model non-uniform distributions of peridynamic points, as might result from a meshing software. Using virtual points also allows the simulation of curved shells, greatly expanding the class of problems that can be approached with this model. Because many analyses of interest are partly or wholly comprised of these types of features, their development is an important addition to the capabilities of peridynamic analysis.

1.2 Outline

The second section of this dissertation reviews the literature for material modeling, focussing on the most prominent PDE-based material failure modeling techniques, alternative nonlocal models, peridynamics, and thin feature modeling. Section 3 provides necessary background information on peridynamic models. Section 4 develops the new bond-pair and bond-multiple peridynamic bending models. Section 5 shows the results of those models for some simple comparison cases. Conclusions and avenues for future development are laid out in Section 6.

Chapter 2: LITERATURE REVIEW

2.1 PDE-Based Failure Modeling

Because material failure is an important part of many problems, there are several computational methods that attempt to simulate progressing material failure. Most of these methods start with the partial differential equations for conservation of momentum found in classical continuum mechanics, then extend those models to account for failure situations that are poorly modeled by the classical equations.

One of the most popular is the eXtended Finite Element Method (XFEM), an excellent overview of which can be found in [28] by Fries and Belytschko. Traditional finite elements use polynomial basis functions to describe unknown fields over an element. As a result, fields such as displacement always vary continuously across an element; discontinuities within an element are poorly approximated even by high-order polynomials. When they are allowed at all, discontinuities can only arise between elements, and are therefore very mesh-dependent; worse, to model a moving or evolving discontinuity requires continual remeshing around the advancing crack tip, adding greatly to the computational complexity of the problem. The finite elements in an XFEM model are “extended” or enriched by adding basis functions that reflect the expected field behavior. In the case of crack growth, this extension comes in the form of discontinuous basis functions. In 1982, Arnold [2] developed a mathematical basis for using discontinuous finite elements and an interior penalty method. This method allows modeling problems with very high gradients (as at boundaries) and greatly reduces the importance of meshing and the need for remeshing. While initially demonstrated for high-gradient heat and fluid flow problems, the method of adding discontinuities within an element had strong potential for failure problems resulting in discontinuous displacements. Instead of remeshing along an expected crack path, a process that would require continual remeshing, the predicted direction of crack growth is used to choose discontinuous basis functions consistent with a crack along that path.

The use of discontinuous basis functions (such as fig. 2.1) to model crack progression through an element was first developed by Belytschko and Black in [6] to model straight and gently curving cracks with less remeshing. The discontinuous function in fig. 2.1 will look familiar. As the transverse displacement field around the tip of a Mode I crack,

$$v(x, y) = \frac{K_I}{2\mu} \sqrt{\frac{r}{2\mu}} \cos\left(\frac{\theta}{2}\right) \left[\kappa - 1 + 2 \sin^2\left(\frac{\theta}{2}\right) \right], \quad (2.1)$$

eq. (2.1) and the other crack-tip displacement fields are a natural choice of basis functions. Longer cracks would require remeshing, but at the root of the crack rather than the tip. Root remeshing represents a major improvement over tip remeshing because it needs to be performed far less frequently. Additionally, the path of the advancing crack can travel at any angle rather than following the angle of a mesh edge. The practice was then extended by Moës et al. in [49] to use different

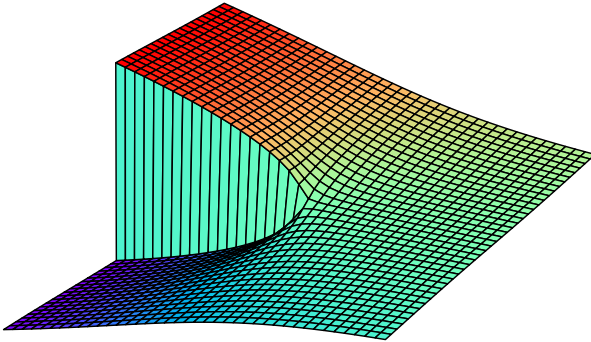


Figure 2.1: XFEM includes discontinuous enrichment basis functions

discontinuous basis functions for cracks and crack tips. Adding a Haar function to model discontinuous displacements far from the crack tip allowed cracks to pass through several elements, enabling the modeling of cracks with greater length and curvature without remeshing.

As with traditional finite element methods, XFEM is mesh-based and uses traditional finite

element basis functions. The elements are enriched extrinsically by adding discontinuous basis functions to the existing basis functions using the Partition of Unity concept described by Melenk and Babuska in [44]. The enrichment functions can capture arbitrary discontinuities in both the parameter being modeled and in its gradient, but the location of the discontinuities must be predicted so that the appropriate enrichment functions can be used. In [49], crack direction was predicted by locating the maximum circumferential stress. There are other options for predicting a crack's direction of travel, but they do not generally predict the formation of a crack where none existed before. Elements are enriched locally as illustrated in fig. 2.2 rather than globally, to capture local phenomena like crack growth. In some elements, every node is enriched, while in others, only some nodes are enriched. Some choices of enrichment functions cause difficulties in the partially enriched “blending” elements, a problem for which a variety of fixes are available depending on the situation.

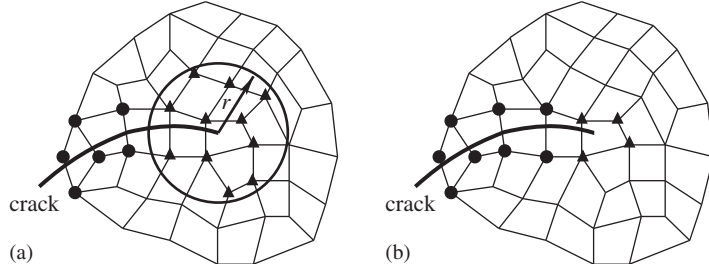


Figure 2.2: XFEM models enrich nodes around a discontinuity [28]

More recently, Sauerland and Fries applied XFEM to two phase flow problems [60], including standard dam-breaking and rising droplet problems. Holl et al. [32] used XFEM in the multi scale modeling of crack propagation, including multiple interacting cracks. Mohammadnejad and Khoei [50] and Hunsweck et al. [33] modeled using XFEM the combination of fluid and fracture behavior found in hydraulic fracturing, a topic of considerable recent interest.

A second common method of modeling material failure is the Reproducing Kernel Particle Method (RKPM), developed by Liu et al. [40]. Mesh-based models track the connections between points in a deforming material, which can become problematic when large deformations deform

the mesh and even cause it to intersect itself. RKPM is a “mesh free” method that tracks material properties by their values at selected points. Mesh-free methods are advantageous for modeling large deformation in fluids and solids because they do not track connections between points. Between material points, properties are interpolated from their values at nearby points by way of integration with a kernel function. The difference in domains between RKPM and XFEM can be seen in fig. 2.3. The key to the RKPM lies in this kernel function; by using window functions from

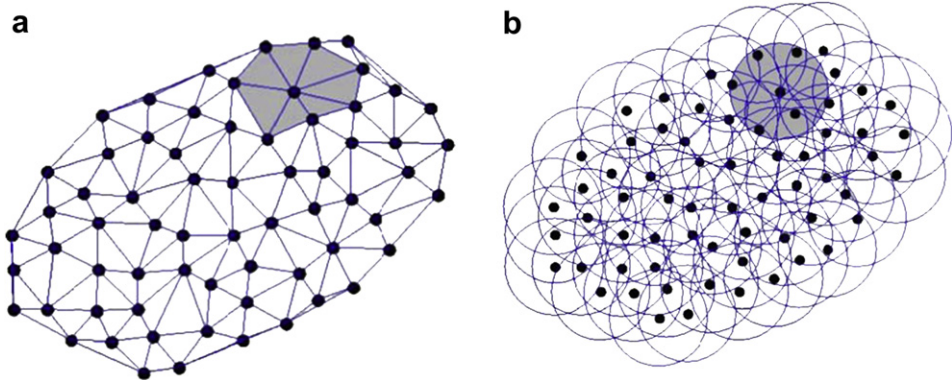


Figure 2.3: Comparison of domains of influence for a)FEM and b)RKPM, by Guan et al. [31]

wavelet analysis, a “reproducing” kernel guarantees that integrals of interpolated properties reproduce the integral of the continuous property field. The “reproducing” kernel makes the RKPM a Partition of Unity method like XFEM, and is a major advantage of RKPM relative to other particle methods. It is, however, computationally expensive.

In its original formulation, the RKPM successfully handles large deformations that would cause unacceptable distortion in Finite Element models. A semi-Lagrangian version implemented by Guan et al. in [30] allows for recalculation of the support function. This allows damage in the form of severing the relationship between points that have been pulled too far apart. Recent applications of the RKPM include the work of Guan et al. on fragment-impact problems [31] and analysis of non-linear wave equations by Cheng and Kim Meow [13]. The RKPM has also been used by Xie and Wang [80] to analyze coupled hydro-mechanical behavior. Wu et al. have coupled RKPM and FEM in their recent work on fragmentation and debris evolution [79].

Other methods of modeling failure include multiple finite element techniques and particle

methods. Finite element methods incorporating “element death” remove from consideration elements that meet particular criteria and are perhaps the simplest way of modeling material failure.

Cohesive zone elements, proposed by Ortiz et al. [55], use element level information to detect the onset of plasticity (material instability) and add suitable deformation modes to model shear banding. The additional deformation modes allow cohesive zone elements to capture the more complex displacements associated with plastic shear bands. Other cohesive zone elements developed by Needleman [53] model crack growth, but Foulk et al. [27] note that this requires very fine meshes or prior knowledge of the crack path. They are useful for cases such as composite delamination or debonding, where the crack follows a known surface. Fang et al. propose in [23] a method of augmenting the cohesive zone model to work in concert with XFEM-type elements to model both arbitrary and known crack paths. More recently, McGarry et al. [43] and Máirtín et al. [41] developed a cohesive zone model to account for crack closure, including crack surface tractions.

Particle methods of modeling failure include the Smooth Particle Hydrodynamic (SPH) method, reviewed by Monaghan in [51], in which a kernel (commonly a cubic spline) is used to create a smooth interpolation of actual quantities. Developed for fluids, Springel notes in [69] that it is often used in astrophysics problems, where many fluid problems are encountered and even “solid” bodies deform under their own gravity. It can also predict elastic behavior and has been extended with failure models by Benz and Asphaug in [7] by adding an evolving damage parameter. Particle methods like SPH handle fragmentation very well, and are used in a variety of problems with material interfaces, high strains, and multiphase and multi-physics aspects. Because cubic spline kernels do not reproduce a Partition of Unity, property interpolation does not accurately reproduce the continuum field. Additionally, elastic SPH models do not conserve angular momentum, and in cases require artificial viscosities or artificial stresses to avoid numerical instability.

The Material Point Method, developed by Sulsky and Schreyer in [70], tracks points in both Eulerian and Lagrangian meshes. The advantage of using both meshes is an ability to handle obstacles and boundary conditions without difficulty at large deformations. Wieckowski notes that

the downside to using both meshes is continual remeshing and added computational expense [78]. Despite this expense, the material point method was extended to model cracks by Nairn in [52], then further enhanced by Sadeghirad et al. in [59] to improve stability when modeling massive deformations. The Lattice Discrete Particle Method was developed by Cusatis et al. [14, 15] to model concrete. It fills a volume with variously-sized particles generated from a probability density function based on aggregate size. The relationships between these particles form tetrahedrons (the lattice) that fill the volume and allow multi-particle interaction. Failure occurs at predefined surfaces between particles and can include various failure modes. The LDPM is capable of accurately modeling many failure conditions in concrete, including the impact of specimen size on effective material behavior. These are only a few of the myriad of models that attempt to model the progression of material failure.

All of these methods are used to solve a partial differential equation for conservation of momentum in a continuum. Because they are based on continuum PDEs, they do not naturally develop discontinuous displacements such as cracks. The PDEs that govern these methods are ill-defined at the surface of a crack, so cracks must be inserted within or between elements after discretization. This results in crack propagation that is discretization-dependent as well as computationally expensive and potentially unstable. Although progress in addressing these issues continues, much of the difficulty is essentially tied to the undefined nature of derivative equations at discontinuous displacements. By abandoning the use of displacement derivatives, peridynamics offers an alternative way to address discontinuous displacements.

2.2 Peridynamic Modeling

The term *peridynamic* was coined by Silling to describe the new formulation of continuum mechanics he developed in [62]. From the Greek roots *peri* and *dyna* meaning *near* and *force* respectively, it alludes to the nonlocal force exerted by nearby points. In contrast to the nonlocal continuum mechanics models of Kröner, Eringen and Edelen [21, 22, 36], the peridynamic model casts material behavior at a point as an *integral* equation of the surrounding displacement rather than the

classical *differential* equation. Because peridynamic models do not include spatial displacement derivatives, discontinuous displacements can arise naturally and can be analyzed without special heuristics. In classical continuum mechanics, linear momentum is conserved according to the local eq. (2.2),

$$\rho(\mathbf{x})\ddot{\mathbf{u}}(\mathbf{x}) = \nabla \cdot \mathbf{P}(\mathbf{x}) + \mathbf{b}(\mathbf{x}) \quad (2.2)$$

in which ρ is the density, $\ddot{\mathbf{u}}$ is the second time derivative of displacement , \mathbf{P} is the transpose of the First Piola Kirchhoff stress tensor, and \mathbf{b} is the body force density, all of which are functions of position \mathbf{x} and of time. Because \mathbf{P} is defined in terms of the deformation gradient, it is clear that eq. (2.2) is undefined for discontinuous displacements. In fact, traditional models require even the first spatial derivative of displacement to be continuous. Strongly nonlocal models (including peridynamics) replace the divergence-of-stress term with an integral functional,

$$\rho(\mathbf{x})\ddot{\mathbf{u}}(\mathbf{x}) = \int_{\Omega} \mathbf{f}(\mathbf{x}, \mathbf{q}) dV_{\mathbf{q}} + \mathbf{b}_{,}(\mathbf{x}) \quad (2.3)$$

so that, instead of the divergence of stress, we have the integral of a “force” function \mathbf{f} of the position vector \mathbf{x} and the position vector \mathbf{q} of a point within the body domain Ω . This force function may depend on \mathbf{x} , \mathbf{q} , their deformed positions, the original and deformed positions of other points in Ω , history, etc. It is common for \mathbf{f} to be defined as 0 for any pair of points initially further than δ apart. The points within δ of a point \mathbf{x} are the *neighborhood* of \mathbf{x} and are denoted in fig. 2.4 by \mathcal{H} . By including the behavior of nearby material, these models introduce an inherent length scale

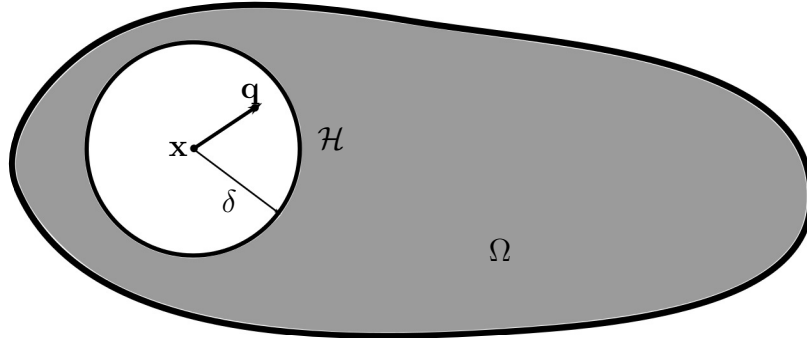


Figure 2.4: A peridynamic body Ω

to the model. This length scale may be determined by material properties or by computational demands.

Constitutive modeling of a wide variety of materials is accomplished by choosing the appropriate form for the force function. While the simplest force functions recreate a one-parameter linear elastic solid material, other force functions can be used to model a wide variety of material behaviors, some of which will be outlined here. Most simulation of material behavior uses an equation of motion reformulated for a discretized model. When discretized, peridynamics is typically a mesh-free numerical method in which there are no geometrical connectivities between various nodes.

A force function can be restricted to being pairwise (depending solely on the displacement of the two points x and q), and still model complex and varied behavior. By including a damage parameter that sets the force contribution of “damaged” bonds to 0, Silling and Askari [66] were able to model a brittle material with natural crack formation, propagation, and branching. Other examples of damage propagation include impacts against brittle structures as in fig. 2.5 modeled by Demmie and Silling [17] and fracturing of thermally-stressed glass modeled by Kilic and Madenci [35]. Modeling progressive fracture, including crack branching, is a major advantage

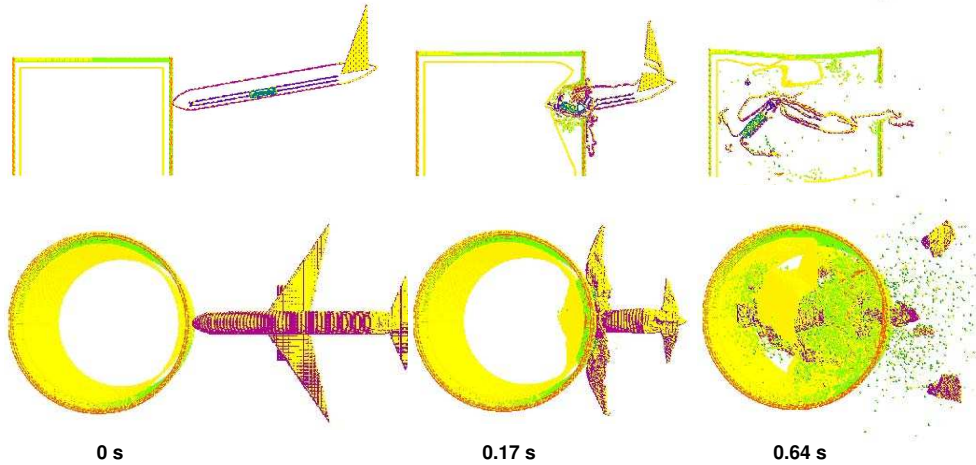


Figure 2.5: Peridynamic model of an airplane impacting a concrete structure [17]

of peridynamic formulations. Using a piecewise force function, Dayal and Bhattacharya [16] were able to model phase transformation in 1D and 2D without an additional constitutive law; the trans-

formations arose and propagated naturally as a dynamic instability, a result of the force function used. Peridynamic models have also been used to analyze composite laminates. In [81], Xu et al. designate peridynamic bonds as fiber or matrix bonds with different force functions to model damage in composite laminates. Kilic et al. model fiber, matrix, and interfacial bonds in [34] to capture stacking order effects on damage propagation. Bobaru [8] applied the peridynamic model to nano fiber networks, at a scale where long-range forces are very apparent. In the same paper he created a Representative Volume Element (RVE) for random networks of nano fibers, laying the ground work for peridynamic multi-scale modeling. Also related to multi-scale peridynamic modeling is work by Silling on model coarsening [63], fig. 2.6. An example of a multi-scale peridynamic simulation can be found in [3], by Askari et al.

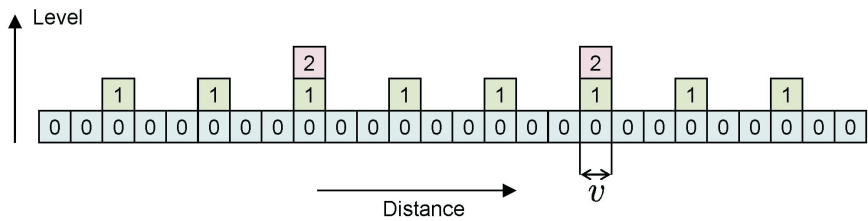


Figure 2.6: Silling's illustration of course-graining in time from [63].

Concrete is a nearly standard example material in which nonlocal behavior is easily observed, and modeling the damage accumulation and proceeding discontinuity propagation has long been the goal of nonlocal models developed by Bazant and Pijaudier-Cabot [5] among others, significantly predating peridynamics. In [29], Gerstle et al. use rotational degrees of freedom to create a concrete material model, capable of describing a linear elastic material with any Poisson ratio, that also handles material failure. Peridynamic models are not limited to force-displacement relationships; the theory has also been applied to diffusion processes and multiphysics problems. Peridynamic models can simulate heat transfer [9] and diffusion [10].

Mathematical analyses of simplified cases have also been fruitful. Weckner [76] determined analytical solutions to the infinite bar problem. Emmerlick and Zimmerman proved solution existence and uniqueness in the simplest case of the peridynamic bar [20]. Mikata found additional analytical solutions for the bar problem [46]. In 3D, Weckner constructed Green's functions for an

infinite peridynamic solid in [77]. All of this work was done with peridynamic models limited to pairwise force functions.

Other than Gerstle’s aforementioned micropolar peridynamic model, the pairwise force function limits 3D solid materials to a Poisson ratio of $\nu = 1/4$. To model additional material behavior, Silling et al. reinvented the underlying peridynamic concept of bonds and forces and introduced state-based peridynamic models in [64]. By freeing the force function from the pairwise restriction, state-based models allow the force relationship between two points to depend on the collective behavior of all nearby material. Using the concept of a deformation vector state allows for the construction of correspondence models that can recreate any classical constitutive model. These correspondence models use the deformation state to approximate the deformation gradient tensor, then use the deformation gradient tensor to calculate force contributions. State-based models were used by Foster et al. to simulate viscoplasticity and hardening in [26], and rate dependent failure in [25], with others, via an energy criterion. Mitchell describes state-based models for plasticity in [47] and viscoelasticity in [48]. A non-ordinary state-based model was used by Warren et al. to simulate fracture in [75]. More recently, Tupek et al. have incorporated the idea of peridynamic damage into a Johnson-Cook based damage state that accumulates with plastic strain [73].

2.3 Other Nonlocal Elasticity Models

The peridynamic formulation of continuum mechanics is neither the only nor the first nonlocal model. Nonlocal elasticity generally allows for forces at a point that are dependent on the material configuration of an entire body, rather than the configuration at that point [22]. While long-range forces are obvious at the molecular model, material at larger scales is conventionally modeled as though internal forces are local or contact forces [36]. The result of such approximation is accurate for deformations that are homogeneous, but introduces some inaccuracy for inhomogeneous deformations like the propagation of waves with short wavelengths. One way to distinguish between homogeneous and inhomogeneous deformations is to incorporate higher-order gradients of deformation. While stress in classical elasticity is a function of the (first) gradient of deformation,

Eringen's formulation of a nonlocal modulus in [21] approximates a weighted sum of the first and second order gradients. This introduces a length scale to the model and has the effect of smearing out local deformation inhomogeneities over the surrounding material, while maintaining the conventional result for homogeneous deformations.

Previous work in the nonlocal mechanics of beams is motivated by the observed stiffening of nanoscale cantilevers. Challamel and Wang demonstrate in [12] that Eringen nonlocal elasticity cannot reproduce the scale stiffening, but that stiffening does result from other gradient-elastic models and models incorporating nonlocal curvature. Because all of these models incorporate higher-order gradients of deformation, they impose stronger continuity requirements than classical elasticity, and are unsuitable for discontinuous displacements. Because the gradients are evaluated locally, gradient models are called *weakly nonlocal*. Recent work by Paolo et al. [56] develops a displacement-based beam in which relative axial displacement, shear displacement, and rotation of non-adjacent beam segments are resisted by three kinds of nonlocal spring, whose stiffnesses can be tuned to the expected material behavior. With the appropriate nonlocal stiffnesses, their model reproduces the nanoscale cantilever stiffening effect.

Similarly, Duan and Wang [19] applied Eringen-type elasticity to the quasi-1D problem of axisymmetric bending in nanoscale plates. Pradhan and Murmu [57] extended the concept to buckling in single-layered graphed sheets, a fully 2D problem. Later, Ansari et al. [1] modeled the vibration of single-layered graphed sheets using Eringen-type elasticity.

Nonlocal effects have also been incorporated into many of the modeling techniques previously discussed. Bazant and Chang incorporated nonlocal strain-softening into a finite element model in [4]. Any interpolating particle method will exhibit some measure of nonlocality, but some explicitly model nonlocal phenomena. Vignjevic et al. used SPH to model nonlocal strain-softening in [74], and in [11], Burghardt et al. developed a material point method that incorporates nonlocal plasticity.

2.4 Thin Features

Many engineering analyses concern shapes that have one dimension much greater than another; numerical modeling the behavior of these shapes can be a considerable challenge for methods designed for 3D solids. In finite element models, for example, calculations can become unstable or too stiff when individual elements become long and thin. To avoid such elements while maintaining model fidelity requires a very large number of solid elements. By making some assumptions about the behavior along the thin direction, many such shapes can be modeled as 1D beams or 2D plates or shells without great loss of accuracy. A comprehensive review of the classical continuum mechanics associated with thin features by Reddy [58] also includes a section on the Finite Element analysis of plates and shells. Material failure in classical thin features is modeled using the same techniques as in solids. Dolbow et al. use XFEM in [18] to model fracture in plates. Li et al. use a variant of RKPM in [37] to model plastic deformation in shells. More recently, Xu et al. have applied XFEM to plate plasticity problems [82], and Memar Ardestani et al. have used RKPM to model functionally graded plates [45]. Other authors use cohesive zone elements [38] or SPH [42] to study failure in thin features.

2.4.1 Peridynamic Models

Reduced dimension thin features such as bars [20,46,67,76], plates [35], and membranes [68] have been modeled using peridynamics, but these models are used for in-plane or membrane forces as shown in fig. 2.7. Because traditional peridynamic models exert forces in the direction of the bonds between points, they are not well-suited for bending problems of thin shapes, in which force and displacement are both nearly perpendicular to bonds connecting material points at separate points on a surface. Just as with solid finite elements, most peridynamic models of thin features like the tubes in fig. 2.8 have included several nodes through the thickness of a thin part to capture bending behavior. Also as with solid finite elements, this leads to very fine discretization of thin features, even when the expected behavior is quite simple. This greatly increases the computational expense

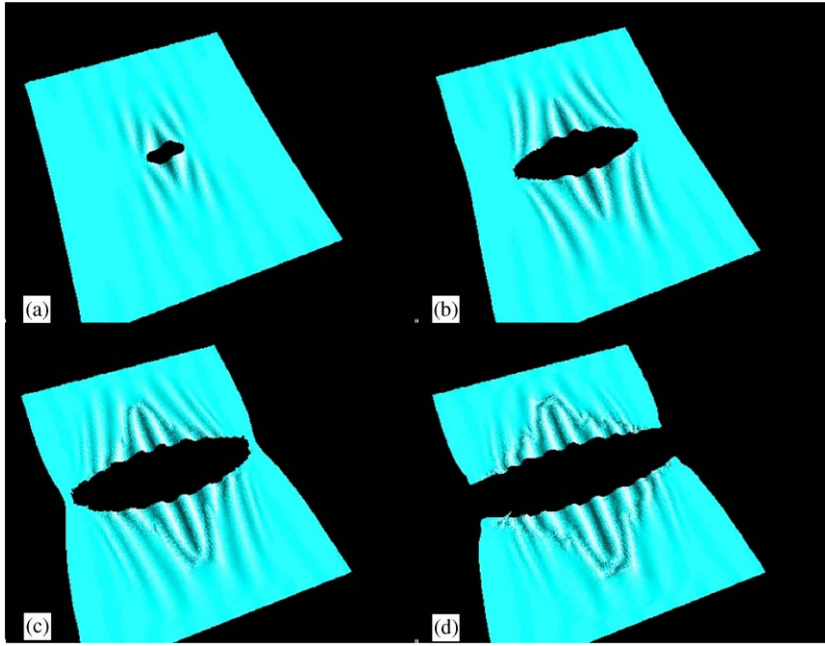


Figure 2.7: Tearing a peridynamic membrane [68]

of modeling parts with thin features.

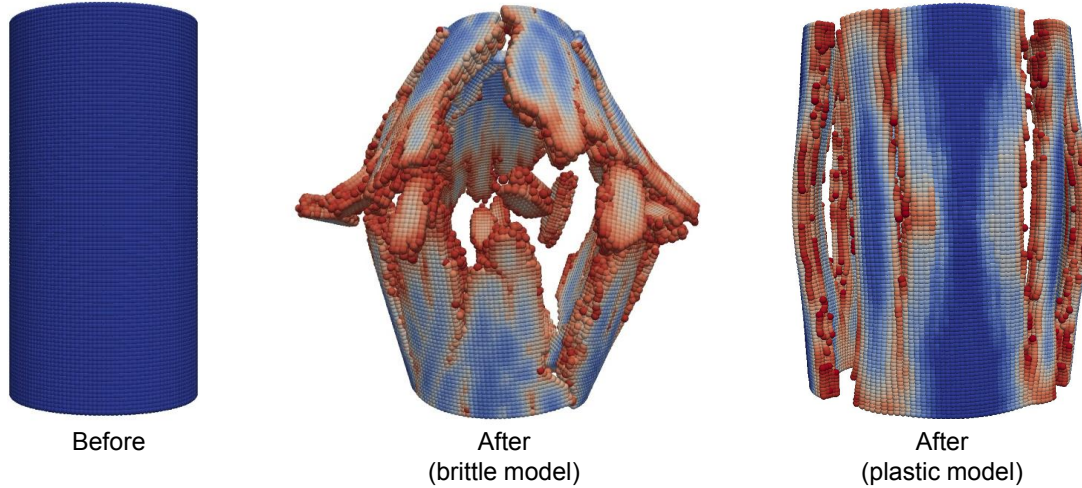


Figure 2.8: A peridynamic cylinder uses several nodes through its thickness in [39]

A recent paper by Taylor and Steigmann [71] partially addresses this issue by starting with mathematical analysis of the continuous 3D bond-based peridynamic solid model of a thin plate. By using a continuous model, they avoid the difficulties associated with discretizing thin features. Applying asymptotic analysis to the continuous model, they reduce a 3D solid model to

2 dimensions. The asymptotic reduction is accomplished by the addition of degrees of freedom for the derivative of displacement with respect to the through thickness direction. By making the through-thickness derivative of displacement vector an independent variable, the resulting flat model includes a measure of angular deformation that allows resistance to bending. Using a simple bond-stretch damage criterion, the Taylor and Steigmann's reduced model was able to capture the out-of-plane displacement (fig. 2.9) associated with crack propagation behavior (fig. 2.10) in a pre-cracked plate under tension loading. In general, however, the asymptotic reduction model encounters difficulty when nonlinear behaviors like damage are implemented. The use of a bond-stretch criterion as implemented is only appropriate when deformation is dominated by in-plane tension, as failure caused by bending will not be captured. Because of its basis in the 3D bond-based solid model, Taylor and Steigmann's model is limited to a Poisson's ratio of $\frac{1}{3}$. While it is possible that future analysis will extend the asymptotic reduction to state-based model, allowing for arbitrary Poisson's ratios, there are significant mathematical hurdles that will have to be overcome.

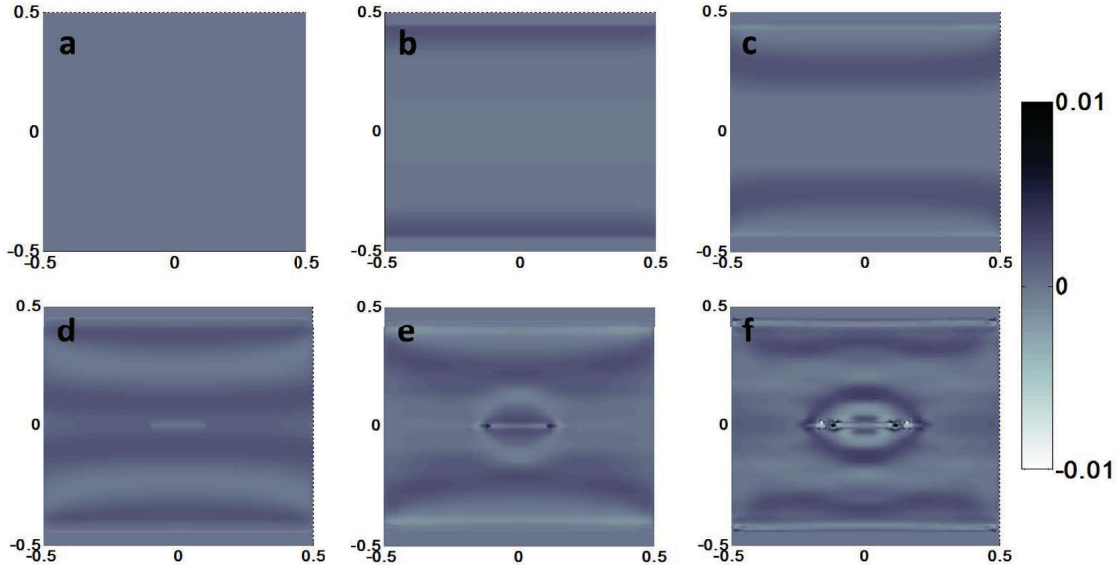


Figure 2.9: Taylor and Steigmann's asymptotic reduction allows for bending resistance in a 2D plate in tension [71]

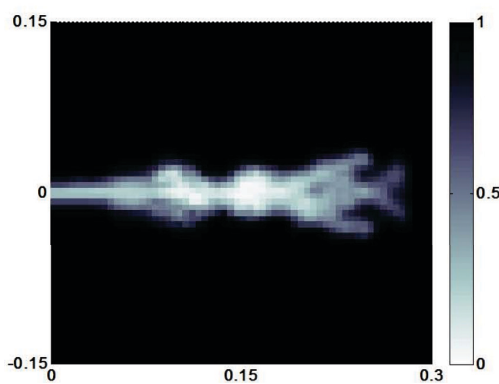


Figure 2.10: Taylor and Steigmann's crack propagation for fig. 2.9 plot **f** [71]

Chapter 3: CLASSICAL BACKGROUND

3.1 Euler-Bernoulli Beam Theory

The simplest representation of bending behavior is found in the Euler-Bernoulli beam equation (eq. (3.1)), which describes the transverse deflection of long-slender beams.

$$\frac{d^2}{dx^2} \left(EI \frac{d^2v}{dx^2} \right) = q \quad (3.1)$$

The equation is for a beam in the \hat{x} direction, whose displacement v is perpendicular to \hat{x} and parallel to the distributed load q acting on the beam. While it is only applicable to small deformations and rotations, there are many problems that can be easily and usefully simplified by the application of Euler beams.

It is important to note that eq. (3.1) is not a constitutive equation; it does not relate stress and strain for a material. Instead, it is derived from the constitutive equation for a linearly-elastic material and some assumptions about the deformation. Euler-Bernoulli beam theory is much simpler than a 3D analysis of a beam as a solid material, but it requires the following assumptions to be met:

- Slenderness: the length of the beam should be 20 times its other dimensions
- Loaded transversely, no axial loads or torques
- Small deformations and rotations
- Plane cross-sections of the beam remain plane under deformation
- Initially straight, and symmetric about the plane of bending

First, we take a infinitesimal slice of a beam as depicted in fig. 3.1. Because we will want to compare to this model later, we use a different y -coordinate direction than many presentations. We use this infinitesimal slice to derive the relationship between load, shear, and moment.

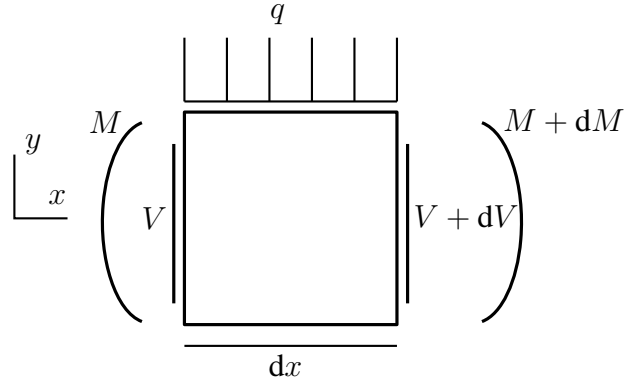


Figure 3.1: Infinitesimal Beam Slice

A force balance demonstrates that the x-derivative of internal shear force is the applied load:

$$V = V + q \, dx + dV \implies \frac{dV}{dx} = -q \quad (3.2)$$

The moment balance can be performed about any point, but it is simplest to use the right side:

$$M - V dx + q \, dx \frac{dx}{2} = M + dM \implies \frac{dM}{dx} = -V + \mathcal{O}(dx) \quad (3.3)$$

Next, we will use the deformation assumptions to frame the bending as a simple arc from which

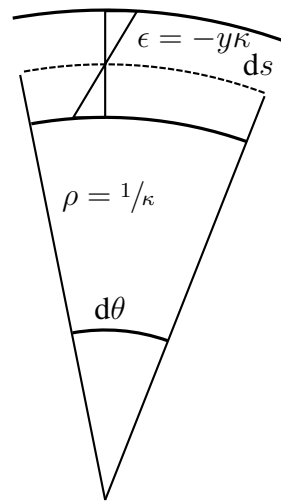


Figure 3.2: Small deformation in an Euler beam

we can deduce a relationship between the transverse displacement of a beam section and its angle

and radius of curvature.

$$\frac{1}{\rho} \approx \frac{d\theta}{dx} \approx \frac{d^2v}{dx^2} = \kappa \quad (3.4)$$

The radius of curvature, ρ is the radius of the arc formed by the beam's neutral axis, which does not change in length as the beam bends. We use this same arc to find the strain in material that is at a distance y from the neutral axis. In a linearly elastic material, the resulting stress is proportional by Young's modulus E . To find the bending moment that results from that stress profile, we integrate the moment contribution through the beam.

$$M_{\text{resisted}} = \int_{\text{bottom}}^{\text{top}} y\sigma dA = \int_{\text{bottom}}^{\text{top}} y^2 E\kappa dA \quad (3.5)$$

In equilibrium, the moment resisted will be equal and opposite to the moment applied.

$$\kappa = \frac{M_{\text{applied}}}{E \int_{\text{bottom}}^{\text{top}} y^2 dA} \quad (3.6)$$

The integral in the denominator is the bending resistance of the beam's shape, called its second moment of area, about the neutral axis. The second moment of area is generally represented by I . By combining eqs. (3.2) to (3.4) and (3.6), we reproduce eq. (3.1), the Euler-Bernoulli beam equation. If the Young's modulus and beam cross section are constant throughout the beam, the equation can be further simplified to

$$EI \frac{d^4v}{dx^4} = q$$

Obviously, to solve for the deformed position we will require 4 constraints from boundary conditions. The nature of the constraints is determined by the support configuration. The most common end conditions are listed table 3.1. Other end constraints, such

End Condition	Constraint 1	Constraint 2
End Load	$w''' = \pm F$	$w'' = 0$
End Torque	$w''' = 0$	$w'' = \pm \tau$
Simply Supported	$w'' = 0$	$w = w_{\text{support}}$
Clamped	$w' = w'_{\text{clamp}}$	$w = w_{\text{clamp}}$

Table 3.1: Common Beam End Conditions

3.2 Kirchhoff-Love Plate Theory

Like Euler-Bernoulli beam theory, Kirchhoff-Love Plate theory begins by making simplifying assumptions about the plate and its deformation.

- Slenderness: the length and width of the plate should be 20 times its thickness
- Loaded transversely, no in-plane loads or torques
- Small deformations and rotations
- Straight lines normal to the plate remain normal to the center plane of the plate under deformation
- Initially flat

These assumptions allow us to simplify our strain-displacement relationships and formulate our curvatures and strains in terms of the transverse displacement w .

$$\kappa_x = \frac{\partial^2 w}{\partial x^2}, \quad \kappa_y = \frac{\partial^2 w}{\partial y^2}, \quad \kappa_{xy} = \frac{\partial^2 w}{\partial x \partial y}$$

$$\varepsilon_x = -z\kappa_x, \quad \varepsilon_y = -z\kappa_y, \quad \gamma_{xy} = -2z\kappa_{xy}$$

To find the stresses at any point, we apply Hooke's law and find

$$\begin{aligned}\sigma_x &= -\frac{Ez}{1-\nu^2} (\kappa_x + \nu \kappa_y) \\ \sigma_y &= -\frac{Ez}{1-\nu^2} (\kappa_y + \nu \kappa_x) \\ \tau_{xy} &= -\frac{Ez}{1+\nu} \kappa_{xy}\end{aligned}$$

As with the beam, these stresses can be integrated over the thickness of the plate to determine the resulting moments.

$$\begin{aligned}M_x &= \int_{-t/2}^{t/2} z \sigma_x dz = -D (\kappa_x + \nu \kappa_y) \\ M_y &= \int_{-t/2}^{t/2} z \sigma_y dz = -D (\kappa_y + \nu \kappa_x) \\ M_{xy} &= \int_{-t/2}^{t/2} z \tau_{xy} dz = -D (1 - \nu) \kappa_{xy}\end{aligned}$$

with

$$D = \frac{Et^3}{12(1-\nu^2)}$$

as the flexural rigidity.

Constructing the governing equation is more complicated than for beams because, instead of shear V and moment M on an infinitesimal section, we have shears V_x and V_y and moments M_x , M_y , and M_{xy} . Balancing forces gives us

$$\frac{\partial V_x}{\partial x} + \frac{\partial V_y}{\partial y} = p \tag{3.7}$$

for transverse pressure p . Balancing moments gives

$$\text{about } x : \quad \frac{\partial M_{xy}}{\partial x} + \frac{\partial M_y}{\partial y} - V_y = 0 \quad (3.8)$$

$$\text{about } y : \quad \frac{\partial M_{xy}}{\partial y} + \frac{\partial M_x}{\partial x} - V_x = 0 \quad (3.9)$$

Combining the force and moment balance equations generates the governing equation

$$\frac{\partial^4 w}{\partial x^4} + 2 \frac{\partial^4 w}{\partial x^2 \partial y^2} + \frac{\partial^4 w}{\partial y^4} = \frac{p}{D} \quad (3.10)$$

As with the beam case, we will need to apply boundary conditions in order to find the deformed configuration.

Chapter 4: PERIDYNAMICS BACKGROUND

4.1 Peridynamic States

Introduced by Silling et al. in 2007 [64], peridynamic states are functions of the behavior of the continuum points surrounding each location. As is appropriate for a theory based on force-carrying bonds, states often operate on vectors. The most common states are scalar-states and vector-states which are scalar and vector valued, respectively. As a matter of convention, scalar states are usually denoted by lowercase letters (e.g. a , b), while vector states are denoted by uppercase letters (e.g. A , B). A state that operates on vectors and is itself vector valued naturally brings to mind a tensor such as the deformation gradient; unlike a second order tensor, which can only map vectors linearly to other vectors, vector-states can produce nonlinear, discontinuous, or even noninvertable mappings. This difference is illustrated in fig. 4.1.

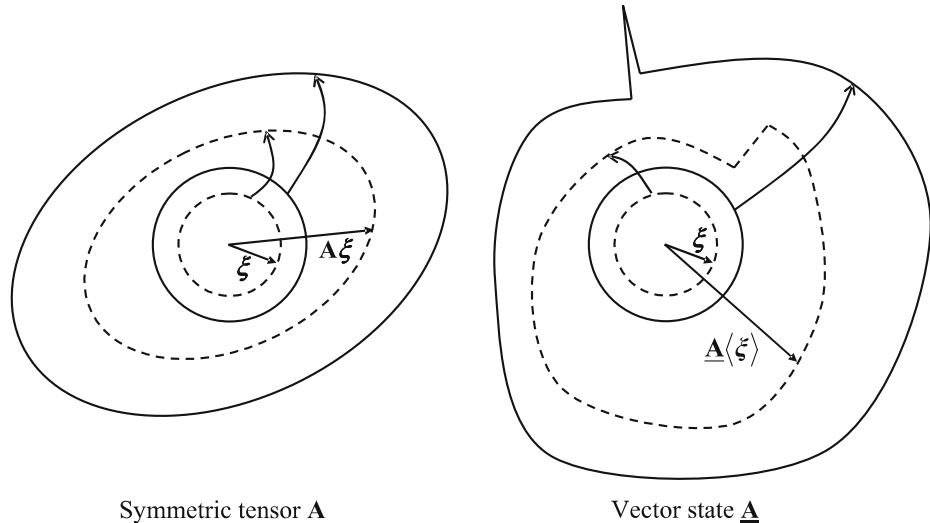


Figure 4.1: The deformation tensor linearly maps spheres to ellipsoids, while a vector state can map spheres nonlinearly to complex and even discontinuous shapes [64]

The mathematical properties of states and several related operators are defined in [64]. Important properties of states are magnitude and direction, while important operations include the addition and composition of states, inner and tensor products, and the Fréchet derivative of a func-

Operation	Notation	Meaning
Addition	$(a + b)\langle \xi \rangle$	$\underline{a}\langle \xi \rangle + \underline{b}\langle \xi \rangle$
Multiplication	$(ab)\langle \xi \rangle$	$\underline{a}\langle \xi \rangle \underline{b}\langle \xi \rangle$
Scalar Product	$(\underline{\mathbf{A}} \cdot \underline{\mathbf{B}})\langle \xi \rangle$	$\underline{\mathbf{A}}\langle \xi \rangle \cdot \underline{\mathbf{B}}\langle \xi \rangle$
Composition	$(\underline{\mathbf{A}} \circ \underline{\mathbf{B}})\langle \xi \rangle$	$\underline{\mathbf{A}}\langle \underline{\mathbf{B}}\langle \xi \rangle \rangle$
Dot Product	$\underline{\mathbf{A}} \bullet \underline{\mathbf{B}}$ $\underline{a} \bullet \underline{b}$	$\int_{\mathcal{H}} \underline{\mathbf{A}}\langle \xi \rangle \cdot \underline{\mathbf{B}}\langle \xi \rangle$ $\int_{\mathcal{H}} \underline{a}\langle \xi \rangle \underline{b}\langle \xi \rangle$
Vector Norm	$ \underline{\mathbf{A}} \langle \xi \rangle$	$ \underline{\mathbf{A}}\langle \xi \rangle $
State Norm	$\ \underline{\mathbf{A}}\ $	$\sqrt{\underline{\mathbf{A}} \bullet \underline{\mathbf{B}}}$
Fréchet Derivative	$\nabla f(\underline{\mathbf{A}})$ $\Psi(\underline{\mathbf{A}}, \underline{\mathbf{B}})_{\underline{\mathbf{A}}}$	$\frac{\partial f}{\partial \underline{\mathbf{A}}}$ $\frac{\partial \Psi}{\partial \underline{\mathbf{A}}}$

Table 4.1: Common State Operation Nomenclature

tion with respect to a state. While some of these operations are intuitive, the nomenclature may not be. Refer to table 4.1 for the notation of common state operations. For a fuller definition and examples of the Fréchet derivative, see appendix A.

4.2 State-based Models

Conservation of linear momentum in the *state-based* peridynamic formulation results in the equation of motion

$$\rho(\mathbf{x})\ddot{\mathbf{u}}(\mathbf{x}) = \int_{\Omega} (\underline{\mathbf{T}}[\mathbf{x}]\langle \mathbf{q} - \mathbf{x} \rangle - \underline{\mathbf{T}}[\mathbf{q}]\langle \mathbf{x} - \mathbf{q} \rangle) dV_{\mathbf{q}} + \mathbf{b}(\mathbf{x}), \quad (4.1)$$

in which $\underline{\mathbf{T}}[]\langle \rangle$ is a *force vector-state* that maps the vector in angle brackets, $\langle \rangle$, originating at the point in square brackets, $[]$, to a force vector acting on that point. The deformed image of the vector $(\mathbf{q} - \mathbf{x})$ is defined as the *deformation vector-state*, usually denoted $\underline{\mathbf{Y}}$ and formulated as shown in eq. (4.2) for a displacement field \mathbf{u} . Just as stress and strain are work conjugate, so too

are the force and deformation vector states for hyperelastic materials.

$$\underline{\mathbf{Y}}[\mathbf{x}]\langle \mathbf{q} - \mathbf{x} \rangle = (\mathbf{q} - \mathbf{x}) + (\mathbf{u}(\mathbf{q}) - \mathbf{u}(\mathbf{x})) \quad (4.2)$$

State-based models include surrounding material behavior illustrated in fig. 4.2 in the force function between each pair of continuum points. It is common for the formulation of the force state $\underline{\mathbf{T}}$ to be scaled by a weighting function, commonly represented by ω , that makes explicit the region in which the force relationship between points is nonzero. Perhaps the simplest and most common weight function is eq. (5.7), representing a constant nonzero value for bonds shorter than the peridynamic horizon δ .

$$\omega(\xi) = \begin{cases} 1 & \text{if } |\xi| \leq \delta \\ 0 & \text{if } |\xi| > \delta \end{cases} \quad (4.3)$$

Many evaluations of forces, energies, and other states at a given point are reduced from being integrals over the entire body to being integrals over that point's neighborhood \mathcal{H} . This is particularly useful when trying to apply peridynamic models to real-world problems, especially when using computer models. If the force state $\underline{\mathbf{T}}$ is always in the same direction as the deformation state

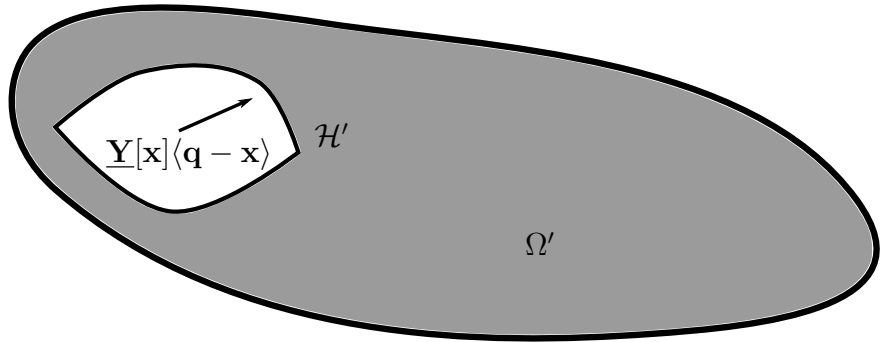


Figure 4.2: The body Ω deformed by the deformation state $\underline{\mathbf{Y}}$

$\underline{\mathbf{Y}}$, then the force exerted by a “bond” between points is in the same direction as the deformed bond, and the model is called *ordinary*. Ordinary state-based can reproduce linear elastic materials with arbitrary Poisson ratios by separating dilatory and deviatoric deformations and the energy corresponding to each. They can also model a variety of elastic and inelastic behaviors.

There is no requirement that force states be in the same direction as their associated deformation states, and models in which they are not in the same direction are called *nonordinary*. Some additional care is needed to ensure that angular momentum is conserved in a *nonordinary* state-based model, but they are still perfectly legitimate. Silling et al. demonstrate the possibility of such models in [65], but very little work has touched on their use. Foster et al. [26] and Warren et al. [75] show that some correspondence models, which approximate the deformation gradient and use it to calculate bond forces, result in non-ordinary state-based constitutive models for finite deformations. Bond-based, ordinary state-based, and nonordinary state-based models are illustrated in fig. 4.3.

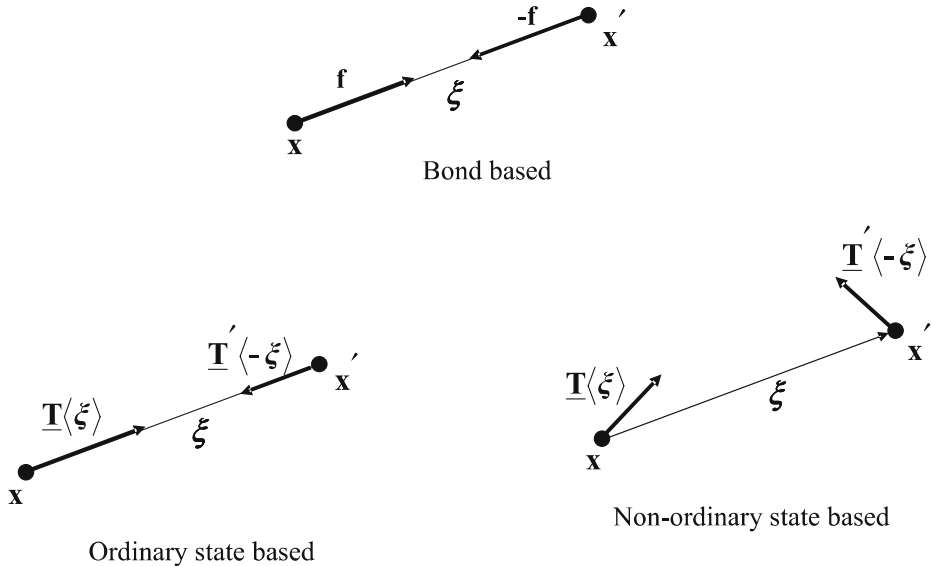


Figure 4.3: Illustration of the three types of peridynamic models, from specific to general [64]

4.3 Bond-based peridynamics

If the force state $\underline{T}[x]\langle\xi\rangle$ depends only on the deformation state $\underline{Y}[x]\langle\xi\rangle$ of the same vector, then the model is called *bond-based*. In *bond-based* peridynamic models, each pair of points is treated separately, without consideration of the behavior of other points. This makes bond-based models much simpler computationally than general state-based models, and reduces the equation of motion

to

$$\rho(\mathbf{x})\ddot{\mathbf{u}}(\mathbf{x}) = \int_{\Omega} \mathbf{f}(\mathbf{u}(\mathbf{q}) - \mathbf{u}(\mathbf{x}), \mathbf{q} - \mathbf{x}) dV_{\mathbf{q}} + \mathbf{b}(\mathbf{x}). \quad (4.4)$$

By choosing an appropriate function \mathbf{f} , this model can reproduce the results of linear elasticity for solid materials with a Poisson ratio $\nu = 1/4$ and 2-dimensional materials with a Poisson ratio $\nu = 1/3$. It can also be used to investigate a range of nonlinear behaviors by changing the force function (examples in fig. 4.4). To conserve momentum in a bond-based model, it is only necessary that \mathbf{f} satisfy

$$\mathbf{f}(\mathbf{u}(\mathbf{q}) - \mathbf{u}(\mathbf{x}), \mathbf{q} - \mathbf{x}) = -\mathbf{f}(\mathbf{u}(\mathbf{x}) - \mathbf{u}(\mathbf{q}), \mathbf{x} - \mathbf{q}), \quad (4.5)$$

i.e. the forces exerted at the opposite ends of the bond between \mathbf{x} and \mathbf{q} must be equal and opposite. The first peridynamic models were all bond-based, and provide useful insight despite their limitations.

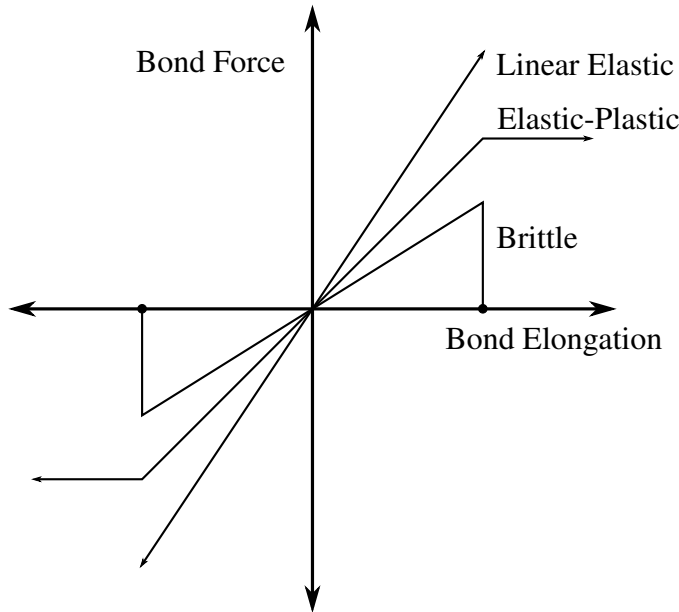


Figure 4.4: Bond-based models can describe a variety of material behaviors

4.4 Important Peridynamic Models

Though they cover only a small portion of the behaviors modeled with peridynamics, these few examples should serve to illustrate the form and analysis of peridynamic material models.

4.4.1 Bond-based Elastic Solid

The simplest peridynamic model treats each bond as a linear spring between two points. In the bond-based formulation, there is no interaction between different bonds, so the force function is

$$\mathbf{f}(\mathbf{u}(\mathbf{q}) - \mathbf{u}(\mathbf{x}), \mathbf{q} - \mathbf{x}) = \omega(|\mathbf{q} - \mathbf{x}|) c s [(\mathbf{q} + \mathbf{u}(\mathbf{q})) - (\mathbf{x} + \mathbf{u}(\mathbf{x}))] \quad (4.6)$$

with weighting function ω , spring constant c , and the stretch s defined by

$$s = |(\mathbf{q} + \mathbf{u}(\mathbf{q})) - (\mathbf{x} + \mathbf{u}(\mathbf{x}))| - |\mathbf{q} - \mathbf{x}|. \quad (4.7)$$

For a small deformation gradient \mathbf{F} , the stretch of bond $\boldsymbol{\xi} = \mathbf{q} - \mathbf{x}$ is

$$s = |\mathbf{F}\boldsymbol{\xi}| - |\boldsymbol{\xi}| = \frac{\epsilon_{ij}\xi_i\xi_j}{|\boldsymbol{\xi}|}$$

For reasons that will become clear in the discussion of the next model, we calibrate the spring constant c following the approach of [64], by comparing the energy to that of a classical solid under purely deviatoric deformation, so that $\epsilon_{ij} = \epsilon_{ij}^d$. The energy of this spring will be in units of Energy per Volume-squared, so that integration over all the springs at a point gives Energy per unit

Volume.

$$\begin{aligned}
w &= \frac{c s^2}{2} \\
W &= \frac{c}{2} \int_{\mathcal{H}} \omega(|\xi|) \left(\frac{\epsilon_{ij}^d \xi_i \xi_j}{|\xi|} \right) \left(\frac{\epsilon_{kl}^d \xi_k \xi_l}{|\xi|} \right) dV_{\xi} \\
&= \frac{c}{2} \epsilon_{ij}^d \epsilon_{kl}^d \int_{\mathcal{H}} \frac{\omega(|\xi|)}{|\xi|^2} \xi_i \xi_j \xi_k \xi_l
\end{aligned} \tag{4.8}$$

Because ω depends only on $|\xi|$, we can rewrite this integral in spherical coordinates as

$$W = \frac{c}{2} \epsilon_{ij}^d \epsilon_{kl}^d \int_0^\delta \frac{\omega(r)}{r^2} \int_0^{2\pi} \int_0^\pi (\xi_i \xi_j \xi_k \xi_l) r^2 \sin(\phi) d\phi d\theta dr$$

Recognizing that $\xi_1 = r \sin \phi \cos \theta$, $\xi_2 = r \sin \phi \sin \theta$, $\xi_3 = r \cos \phi$, we can see that configurations of $[i, j, k, l]$ with an odd number of any index result in integrals with an odd number of one or more of $\cos \theta$, $\sin \theta$, $\cos \phi$, and therefore are equal to 0. For the remaining configurations,

$$\int_0^\delta \frac{\omega(r)}{r^2} \int_0^{2\pi} \int_0^\pi (r^4 \sin^4 \phi \cos^2 \theta \sin^2 \theta) r^2 \sin(\phi) d\phi d\theta dr = \frac{4\pi}{15} \int_0^\delta \omega(r) r^4 dr$$

Also, any combination with $i = j$ or $k = l$ results in terms ϵ_{ii}^d or ϵ_{kk}^d , which will sum to 0 in deviatoric deformation. This leaves only configurations such as $[1, 2, 1, 2]$ and $[3, 2, 2, 3]$, which we can indicate by $(\delta_{ik}\delta_{jl} + \delta_{il}\delta_{jk})$.

$$\begin{aligned}
W &= \frac{c}{2} \epsilon_{ij}^d \epsilon_{kl}^d \frac{4\pi}{15} \int_0^\delta \omega(r) r^4 dr (\delta_{ik}\delta_{jl} + \delta_{il}\delta_{jk}) \\
&= c \epsilon_{ij}^d \epsilon_{ij}^d \frac{4\pi}{15} \int_0^\delta \omega(r) r^4 dr \\
&= \frac{c \epsilon_{ij}^d \epsilon_{ij}^d}{15} m
\end{aligned}$$

To force the result to be independent of the horizon δ , we normalize the expression by

$$m = \int_{\mathcal{H}} \omega(|\xi|) |\xi|^2 = 4\pi \int_0^\delta \omega(r) r^4 dr \tag{4.9}$$

By comparing to the classical strain energy density $\Omega = G \epsilon_{ij}^d \epsilon_{ij}^d$ for shear modulus G , we can determine the appropriate bond stiffness

$$c = \frac{15 G}{m}$$

Applying a purely dilational deformation to the same model is far easier. With dilation θ , the stretch of a bond in any direction is

$$s = \frac{\theta}{3} r,$$

and the corresponding energy is

$$\begin{aligned} W &= \frac{c}{2} \int_{\mathcal{H}} \omega(|\xi|) \frac{\theta^2}{9} r^2 dV_\xi \\ &= \frac{c \theta^2}{18} \int_0^\delta \omega(r) \int_0^{2\pi} \int_0^\pi r^2 r^2 \sin(\phi) d\phi d\theta dr \\ &= \frac{c \theta^2}{18} m \\ &= \frac{15}{9} G \frac{\theta^2}{2} \end{aligned} \tag{4.10}$$

This shows that the model based on bond-stretch has a bulk modulus that is $15/9$ of its shear modulus, indicating a Poisson's ratio of $1/4$.

A nearly identical analysis can be performed on a simpler 2D version of the same model, departing after eq. (4.8). Applying a purely deviatoric in-plane shear to such a model, and comparing the resulting energy to that of a classical plate with thickness t gives us

$$c = \frac{8 G t}{m_{2D}}; \quad m_{2D} = \int_{\mathcal{H}_{2D}} \omega(|\xi|) |\xi|^2.$$

Applying a planar dilation deformation to a 2D plate results in strain energy consistent with a Poisson's ratio of $1/3$ rather than the value of $1/4$ found for the 3D solid.

4.4.2 State-based Elastic Solid

The state-based linear isotropic peridynamic solid material model is both important and illustrative. Developed in [64], it uses many of the important characteristics of peridynamic states to model a linearly-elastic material with any valid Poisson's ratio. The extension state \underline{e} is exactly the same as the stretch s in eq. (4.7). Classical material models dealing with metal plasticity often separate deformation into dilation and deviatoric components. Similarly, the extension state can be decomposed into isotropic and deviatoric extension states. Using m from eq. (4.9) as above for normalization the dilation state is defined

$$\theta = \frac{3}{m} \int_{\mathcal{H}} \omega(\xi) |\xi| \underline{e}. \quad (4.11)$$

The isotropic and deviatoric extension states are defined in turn

$$\underline{e}^i = \frac{\theta |\xi|}{3}, \quad \underline{e}^d = \underline{e} - \underline{e}^i \quad (4.12)$$

If the energy associated with dilation is set to

$$W^i = \frac{k \theta^2}{2},$$

then the corresponding force state and peridynamic pressure are

$$\underline{t} = \frac{3k\theta}{m} \omega(\xi) |\xi|, \quad p = -k\theta$$

We saw in the analysis of the bond-based model the necessary bond stiffness to match the energy associated with purely deviatoric deformation. The two can be combined for eq. (4.13), a force state that clearly indicates the separate responses to dilation and deviatoric deformation.

$$\underline{t} = \frac{3k\theta}{m} \omega(\xi) |\xi| + \frac{15G}{m} \omega(\xi) \underline{e}^d \quad (4.13)$$

A quick examination shows that, in the case that the dilation θ is not constant, the force at either end of a bond will not satisfy eq. (4.5). Thus such a model is not possible in a bond-based framework without significant modification.

4.4.3 Correspondence Models

One way to create a peridynamic material model is to start from a material model in classical dynamics. Classical models based on the deformation gradient have the advantage of decades of development and tens of thousands of hours of testing, and they enjoy widespread use in the continuum mechanics community. Peridynamic *correspondence* models use the relative positions of a points neighbors to determine $\bar{\mathbf{F}}(\underline{\mathbf{Y}})$, a nonlocal approximation of the deformation gradient \mathbf{F} .

$$\bar{\mathbf{F}}(\underline{\mathbf{Y}}) = \left[\int_{\mathcal{H}} \omega(|\xi|)(\underline{\mathbf{Y}} \langle \xi \rangle \otimes \xi) dV_\xi \right] \bar{\mathbf{K}}^{-1} \quad (4.14)$$

with the shape tensor $\bar{\mathbf{K}}$ defined by

$$\bar{\mathbf{K}} = \int_{\mathcal{H}} \omega(|\xi|)(\xi \otimes \xi) dV_\xi$$

When \mathbf{F} is constant, $\bar{\mathbf{F}}(\underline{\mathbf{Y}})$ is exactly equal to \mathbf{F} . If the classical model in question is hyperelastic with energy density $\Omega(\mathbf{F})$, it is a simple matter to force the peridynamic model to have identical energy by defining

$$W(\underline{\mathbf{Y}}) = \Omega(\bar{\mathbf{F}}(\underline{\mathbf{Y}})) \quad (4.15)$$

and find the force vector state by taking the Fréchet derivative of W with respect to $\underline{\mathbf{Y}}$. Alternately, the classical continuum model can be applied to find the first Piola-Kirchhoff stress σ associated with $\bar{\mathbf{F}}$:

$$\sigma = \frac{\partial \Omega(\bar{\mathbf{F}})}{\partial \bar{\mathbf{F}}} \quad (4.16)$$

The resulting force state is calculated from the stress according to

$$\underline{\mathbf{T}}\langle \boldsymbol{\xi} \rangle = \omega(\boldsymbol{\xi}) \boldsymbol{\sigma} \mathbf{K}^{-1} \boldsymbol{\xi} \quad (4.17)$$

For homogenous deformations, the result is a peridynamic model that exactly reproduces the classical model without ever taking a derivative. For problems with very inhomogenous (on the scale of the peridynamic horizon) deformations, the peridynamic model will exhibit scale effects not seen in the classical model, acting to smooth out the effect of short-scale deformations. For discontinuous deformations, the classical model cannot be evaluated at all, but the peridynamic correspondence model will have no such problem. It may be necessary however to revisit the choice of model or implement some damage condition.

Chapter 5: MODEL DEVELOPMENT

5.1 Bond Pair Material Model

Consider the material model illustrated in fig. 5.1 in which every bond-vector originating from a point is connected by a rotational spring to its opposite originating from that same point. If we call

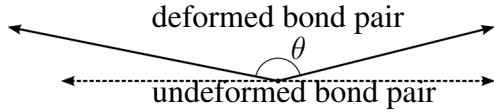


Figure 5.1: Illustration of a bond pair model that resists angular deformation

the deformed angle between these bonds θ , and choose the potential energy of that spring to be $w(\xi) = \omega(\xi)\alpha[1 + \cos(\theta)]$ for the bond pair ξ and $-\xi$, we can recover the non-ordinary force state proposed by Silling in [64] by taking the Fréchet derivative. For the derivation and a description of the Fréchet derivative see appendix A.

$$\begin{aligned} \underline{\mathbf{T}}\langle\xi\rangle &= \nabla w(\underline{\mathbf{Y}}\langle\xi\rangle) \\ &= \omega(\xi) \frac{-\alpha}{|\underline{\mathbf{Y}}\langle\xi\rangle|} \frac{\underline{\mathbf{Y}}\langle\xi\rangle}{|\underline{\mathbf{Y}}\langle\xi\rangle|} \times \left[\frac{\underline{\mathbf{Y}}\langle\xi\rangle}{|\underline{\mathbf{Y}}\langle\xi\rangle|} \times \frac{\underline{\mathbf{Y}}\langle-\xi\rangle}{|\underline{\mathbf{Y}}\langle-\xi\rangle|} \right] \end{aligned} \quad (5.1)$$

Though it looks complex, eq. (5.1) indicates a bond force perpendicular to the deformed bond and in the plane containing both the deformed bond and its partner as illustrated in fig. 5.2. The force magnitude is proportional to the sine of the angle between the bonds divided by the length of the deformed bond. This response is consistent with the idea of a rotational spring between bonds as

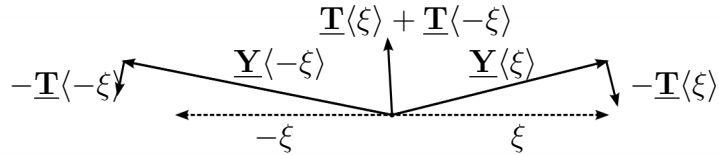


Figure 5.2: Deformation and force vector states

long as the change in angle is small. Because the potential energy and force states are functions

of pairs of peridynamic bonds, we will call this formulation a *bond-pair model*. Other choices for the bond-pair potential function, such as $w = (\pi - \theta)^2$, are also possible, but result in more mathematically complex analysis.

5.2 Bond Pair Beam in Bending

The simplest application of our bond-pair based peridynamic model is that of fig. 5.3, a beam in transverse bending. Much of the material in this section can also be found in [54].

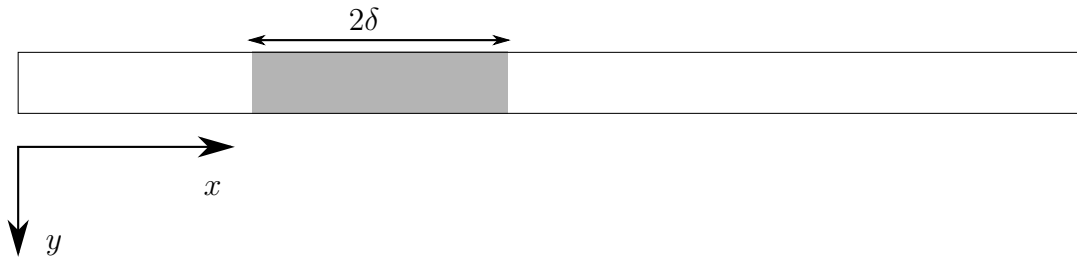


Figure 5.3: A continuous peridynamic beam with horizon δ

5.2.1 Energy Equivalence

To determine an appropriate choice of α for eq. (5.1), we desire our peridynamic model to have an equivalent strain energy density to a classical Euler-Bernoulli beam in the *local limit*, i.e. when the nonlocal length scale vanishes. We will begin with the assumptions from Euler beam theory: the length of the beam is much greater than thickness, vertical displacements are small, and rotations are small. For small vertical displacements (i.e. $\sin \theta \approx \theta$) we have

$$\theta(\underline{\mathbf{Y}}\langle\xi\rangle, \underline{\mathbf{Y}}\langle-\xi\rangle) \approx \pi - \frac{v(x + \xi) - 2v(x) + v(x - \xi)}{\xi}, \quad (5.2)$$

where v is the vertical displacement of material point. Momentarily assuming that v is continuous and using a Taylor series to expand the right-hand-side of eq. (5.2)

$$\begin{aligned}\theta(\underline{\mathbf{Y}}\langle\xi\rangle, \underline{\mathbf{Y}}\langle-\xi\rangle) &\approx \pi - \xi \frac{\partial^2 v}{\partial x^2} + \mathcal{O}(\xi^3) \\ &\approx \pi - \xi \kappa + \mathcal{O}(\xi^3);\end{aligned}\quad (5.3)$$

with

$$\kappa = \frac{\partial^2 v}{\partial x^2}.$$

Substituting eq. (5.3) into the equation for the strain energy density of a single bond-pair,

$$\begin{aligned}w(\xi) &= \omega(\xi)\alpha [1 + \cos(\theta(\underline{\mathbf{Y}}\langle\xi\rangle, \underline{\mathbf{Y}}\langle-\xi\rangle))] \\ &\approx \omega(\xi)\alpha \frac{\xi^2}{2} (\kappa)^2 + \mathcal{O}(\xi^4).\end{aligned}$$

If we use a weighting function $\omega(\xi) = \omega(|\xi|)$ and assume that the ω plays the role of a localization kernel, i.e. $\omega = 0 \forall \xi > \delta$, the resulting strain energy density, W , for any material point in the peridynamic beam is

$$W = \frac{\alpha}{2} \kappa^2 \int_{-\delta}^{\delta} \omega(\xi) \xi^2 d\xi + \mathcal{O}(\delta^5).$$

Equating W with the classical Euler-Bernoulli beam strain-energy density, Ω , and taking the limit as $\delta \rightarrow 0$ we can solve for α

$$\begin{aligned}\lim_{\delta \rightarrow 0} W &= \Omega, \\ \frac{\alpha}{2} m \kappa^2 &= \frac{EI}{2} \kappa^2, \\ \alpha &= \frac{EI}{m},\end{aligned}\quad (5.4)$$

with

$$m = \int_{-\delta}^{\delta} \omega(\xi) \xi^2 d\xi.$$

While this demonstrates the model's equivalence to a linearly-elastic Euler beam, if we keep an additional term from the Taylor series approximation of eq. (5.2), we recover a slightly more complex expressions for change in angle that is demonstrated in 5.2.2 to reproduce an Euler beam governed by Eringen's model of nonlocal elasticity.

5.2.2 Relation to Eringen Nonlocality

If we keep an additional term from the Taylor series approximation of eq. (5.2), we recover a slightly more complex expressions for change in angle

$$\theta(\underline{\mathbf{Y}}\langle\xi\rangle, \underline{\mathbf{Y}}\langle-\xi\rangle) \approx \arctan\left(\pi - \xi \frac{\partial^2 v}{\partial x^2} - \frac{\xi^3}{12} \frac{\partial^4 v}{\partial x^4} + \mathcal{O}(\xi^5)\right)$$

and for the strain energy (again substituting $\kappa = v''$ for readability),

$$W \approx \int_{-\delta}^{\delta} \omega(\xi) \alpha \left(\frac{\xi^2}{2} \kappa^2 + \frac{\xi^4}{12} \kappa \kappa'' - \frac{3}{8} \frac{\xi^4}{\kappa^4} + \mathcal{O}(\xi^6) \right) d\xi.$$

As the horizon δ becomes small, higher-order ξ terms become relatively less important, and $\xi^4 \kappa^4$ is dominated by $\xi^2 \kappa^2$ for large κ and by $\xi^4 \kappa \kappa''$ for small κ . The remaining terms can be rearranged,

$$W \approx \int_{-\delta}^{\delta} \omega(\xi) \alpha \frac{\xi^2}{2} \kappa \left(\kappa + \frac{\xi^2}{6} \kappa'' \right) d\xi,$$

in a manner strongly suggesting an alternative bending resistance term. We can picture a bending resistance based on the bond length and proportional to the nonlocal curvature $\bar{\kappa} = (\kappa + \frac{\xi^2}{6} \kappa'')$, so that

$$\begin{aligned} \bar{\kappa} &= \left(\kappa + \frac{\xi^2}{6} \kappa'' \right) \implies \\ W &\approx \int_{-\delta}^{\delta} \omega(\xi) \alpha \frac{\xi^2}{2} \kappa \bar{\kappa} d\xi. \end{aligned} \tag{5.5}$$

The same analysis can be taken further to obtain higher-order energy terms with even powers of ξ and even order derivatives of κ . Not all of these higher-order terms can be separated into the product of a local curvature and nonlocal bending resistance.

Eringen's model for nonlocal elasticity in [21] begins with a nonlocal modulus (denoted here as $K(|\mathbf{x}' - \mathbf{x}|, \tau)$) that relates the nonlocal stress \mathbf{t} at a point to the classical (local) stress $\boldsymbol{\sigma}$ in the nearby material through the integral

$$\mathbf{t} = \int_V K(|\mathbf{x}' - \mathbf{x}|, \tau) \boldsymbol{\sigma}(\mathbf{x}') dv(\mathbf{x}').$$

In the local limit these relationships take the form of higher-order gradients. Using a 1-dimensional decaying exponential nonlocal modulus $K(|x|, \tau) = \frac{1}{l\tau} e^{-\frac{|x|}{l\tau}}$ results in a relationship between t_{1D} and σ_{1D}

$$\left(1 - \tau^2 l^2 \frac{\partial^2}{\partial x^2}\right) t_{1D} = \sigma_{1D},$$

in which $\tau^2 l^2$ is a scale-based material parameter. For well-behaved t_{1D} and σ_{1D} and small values of σ_{1D}''' and $\tau^2 l^2$, we can see that this relationship could be reformulated as

$$t_{1D} = \left(1 + \tau^2 l^2 \frac{\partial^2}{\partial x^2}\right) \sigma_{1D}.$$

If we consider the results of the previous section and let $dM = y\sigma dA$ and $\sigma = E y \kappa$, the contribution to moment resulting from Eringen's nonlocal elasticity in a fiber at y

$$E y^2 (\kappa + \tau^2 l^2 \kappa''), \quad (5.6)$$

and the resulting strain energy

$$\int_{-\frac{t}{2}}^{\frac{t}{2}} b(y) E \frac{y^2}{2} \kappa (\kappa + \tau^2 l^2 \kappa'') dy,$$

bear a striking resemblance to eq. (5.5). In fact, by carefully choosing peridynamic parameter values, the results can be made identical. For a rectangular beam of width b and thickness t , choosing

$$\omega(\xi) = |\xi|b; \quad \delta = \tau l \sqrt{3}; \quad \alpha = \frac{Ebt^3}{54\tau^4 l^4}$$

results in

$$W \approx Eb \frac{t^3}{12} \frac{\kappa}{2} (\kappa + \tau^2 l^2 \kappa''),$$

the same result for both models.

The similarity between eqs. (5.5) and (5.6) is not accidental; Eringen's gradient elasticity is the solution to the integral formulation of the nonlocal stress integral equation just as the peridynamic energy is an integral function of nonlocal displacements. It is therefore unsurprising that, like Eringen's nonlocal elasticity [12], this peridynamic bending model fails to predict the stiffening associated with nanoscale cantilevers. Instead, the advantage of peridynamic models is their natural handling of discontinuities.

5.2.3 Weighting function and inelasticity

The weighting function $\omega(\xi)$ describes the relative contribution of each bond-pair, and can be defined according to physical or mathematical considerations. While any function $\omega(\xi)$ that produces a convergent integral for m will reproduce an elastic Euler beam, a physically meaningful choice of ω will allow us to extend our model to certain inelastic behaviors. Consider a classical Euler-Bernoulli beam in bending with curvature κ . Fibers running parallel to the neutral axis of the beam are stretched in proportion to their distance from the neutral axis, with strain $\epsilon = y\kappa$. If the fibers are linearly elastic, then the axial stress at each location is $\sigma = E\epsilon = Ey\kappa$, and the contribution to supported moment $dM = \kappa E y^2 dA$. By comparing the formulations for the moments carried by the Euler beam in fig. 5.4 and those of the bond-pair beam in fig. 5.5, we see some definite parallels.

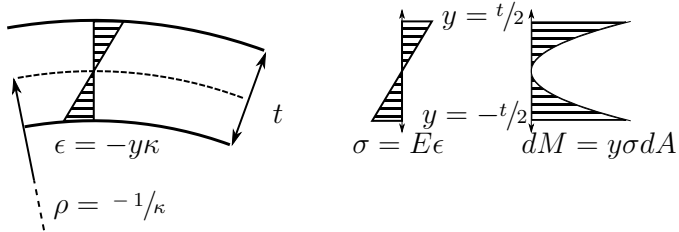


Figure 5.4: Euler beam moment contribution

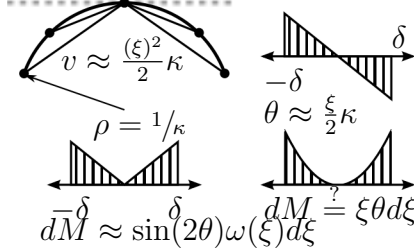


Figure 5.5: Bond-pair moment contribution

$$\begin{aligned}
 M_E &= \int_{-\frac{t}{2}}^{\frac{t}{2}} \sigma y \, dA & &= \int_{-\frac{t}{2}}^{\frac{t}{2}} E\kappa y^2 b(y) dy \\
 M_{PD} &= \int_{-\delta}^{\delta} \underline{\mathbf{T}}\langle\xi\rangle \xi \, d\xi & & \\
 &= \int_{-\delta}^{\delta} \alpha \frac{\sin(\Delta\theta)}{|\xi|} \xi \omega(\xi) d\xi & & \approx \int_{-\delta}^{\delta} \alpha\kappa|\xi| \omega(\xi) d\xi
 \end{aligned}$$

The term y is the distance from the beam's neutral axis and $b(y)$ is the width of the beam at that distance from the neutral axis. The similarity between classical and peridynamic moment formulations suggests a possible formulation for the weighting function:

$$\omega(\xi) = |\xi|b(y) \quad \text{at} \quad y = \frac{\xi t}{\delta 2} \quad (5.7)$$

This weight function analogizes the relative contributions of bond pairs of different lengths to the relative contributions of fibers at different distances from the centerline. An example for a rectangular beam is illustrated in fig. 5.6. For an I beam with height h_{beam} , width w_{beam} , web height

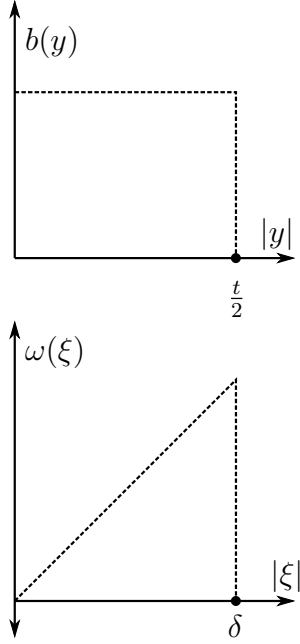


Figure 5.6: Weight function for a beam of rectangular cross-section

h_{web} , and web width w_{web} , substituting the beam profile

$$b(y) = \begin{cases} w_{\text{web}} & \text{if } |y| \leq \frac{h_{\text{web}}}{2} \\ w_{\text{beam}} & \text{if } \frac{h_{\text{web}}}{2} < |y| \leq \frac{h_{\text{beam}}}{2} \\ 0 & \text{otherwise} \end{cases}$$

into eq. (5.7) gives the weight function

$$\omega(\xi) = \begin{cases} |\xi|w_{\text{web}} & \text{if } |\xi| \leq \delta \frac{h_{\text{web}}}{h_{\text{beam}}} \\ |\xi|w_{\text{beam}} & \text{if } \delta \frac{h_{\text{web}}}{h_{\text{beam}}} < |\xi| \leq \delta \\ 0 & \text{otherwise} \end{cases}$$

and is illustrated in fig. 5.7. While this weighting function offers no advantages over a uniform weight function in the case of the linearly elastic beam, it offers a way to model advancing plasticity.

In a deformed elastic perfectly-plastic beam, axial fibers are still stretched in proportion to their

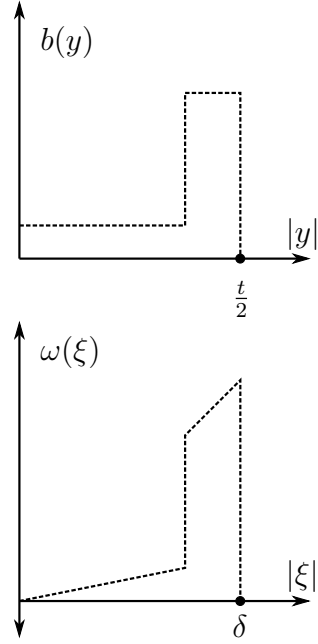


Figure 5.7: Weight function for an I-beam

distance from the neutral axis, but the relationship $\sigma = E\epsilon = Ey\kappa$ only holds for $|\epsilon| = |y\kappa| < \epsilon_c$.

For greater stretches, the relationship becomes $\sigma = \pm E\epsilon_c$. To model this behavior, consider a bond pair with similar behavior: for angular deformation less than some critical angle, the model behaves as previously described, but the magnitude of the force remains constant above a critical deformation

$$|\underline{\mathbf{T}}(\xi)| = \begin{cases} \alpha\omega(\xi) \frac{\sin(\theta(\underline{\mathbf{Y}}(\xi), \underline{\mathbf{Y}}(-\xi)))}{|\underline{\mathbf{Y}}(\xi)|} & \text{if } \theta < \theta_c \\ \alpha\omega(\xi) \frac{\sin(\theta_c)}{|\underline{\mathbf{Y}}(\xi)|} & \text{if } \theta \geq \theta_c \end{cases} \quad (5.8)$$

to determine the critical angle θ_c , we let the onset of plasticity in pairs of the longest bonds to coincide with the onset of plasticity in the fibers at the top and bottom surfaces of the classical beam. For small curvatures $\Delta\theta = \xi\kappa \implies \Delta\theta_c = \frac{2\delta\epsilon_c}{t}$. For curvatures $|\kappa| > \kappa_c = \frac{2\epsilon_c}{t}$, the radius within which bonds are in the elastic region is $\delta_e = \delta\kappa_c$, and parallels the distance from the beam

centerline that fibers are in the elastic region $y_e = \frac{t}{2} \frac{\kappa_c}{\kappa}$

$$M_{\text{classical}} = 2 \int_0^{y_e} Eb(y) y^2 \kappa dy + 2 \int_{y_e}^{\frac{t}{2}} Eb(y) \epsilon_c y dy$$

$$M_{\text{PD}} = 2 \int_0^{\delta_e} \alpha \omega(\xi) \xi^2 \kappa d\xi + 2 \int_{\delta_e}^{\delta} \alpha \omega(\xi) \Delta \theta_c \xi d\xi$$

Of course, as long as the force is independent of history, this model only represents a nonlinear elastic material. By keeping track of the plastic deformation $\theta^p(\xi) = \theta - \theta_c$ of each bond-pair, and applying it as an offset, we can reproduce the hysteresis associated with elastic-perfectly-plastic deformation.

More simply, we can model a brittle material by setting the force to zero for bond pairs exceeding a critical angle,

$$|\underline{\mathbf{T}}(\xi)| = \begin{cases} \alpha \omega(\xi) \frac{\sin(\theta(\underline{\mathbf{Y}}(\xi), \underline{\mathbf{Y}}(-\xi)))}{|\underline{\mathbf{Y}}(\xi)|} & \text{if } \theta < \theta_c \\ 0 & \text{if } \theta \geq \theta_c \end{cases} \quad (5.9)$$

and additionally recording bond pairs that have exceeded their critical angle and permanently setting their influence, i.e. ω , to zero.

5.3 Bond Pair Plate in Bending

The next case we will analyze is the extension of the bond pair beam model to fig. 5.8, a flat plate in the xy plane, with displacement w in the z -direction.

5.3.1 Energy Equivalence

As with the beam model, we determine an appropriate choice of α so that our peridynamic model will have an equivalent strain energy density to a classical Kirckhoff plate in the *local limit*. We will begin with the assumptions from Kirckhoff plate theory: straight lines normal to the mid-surface remain both straight and normal to the deformed mid-surface, and the plate thickness does not change with deformation. As with the Euler beam energy equivalence, we will start with the

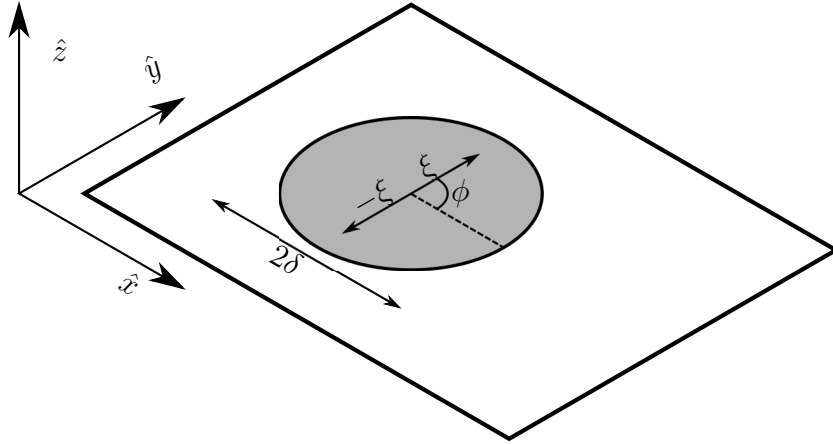


Figure 5.8: Illustration of a bond pair on a plate.

original assumptions from Kirchhoff-Love plate theory of small displacements and rotations, but they will not constrain the validity of the model for larger displacements and rotations. For small vertical displacements we have

$$\theta(\underline{\mathbf{Y}}\langle\xi\rangle, \underline{\mathbf{Y}}\langle-\xi\rangle) \approx \pi - \frac{w(\mathbf{x} + \xi) - 2w(\mathbf{x}) + w(\mathbf{x} - \xi)}{|\xi|}, \quad (5.10)$$

where w is the vertical displacement of material point. Taking $\xi = \xi(\cos(\phi), \sin(\phi))$ in cartesian coordinates and momentarily assuming continuous displacements for the sake of comparison, we use a Taylor series to expand the right-hand-side of eq. (5.10) about $\xi = 0$

$$\theta(\underline{\mathbf{Y}}\langle\xi\rangle, \underline{\mathbf{Y}}\langle-\xi\rangle) \approx \pi - \frac{\xi}{2} (\cos^2(\phi)\kappa_1 + \sin^2(\phi)\kappa_2 + 2\sin(\phi)\cos(\phi)\kappa_3) + \mathcal{O}(\xi^3) \quad (5.11)$$

with

$$\kappa_1 = \frac{\partial^2 w}{\partial x_1^2}, \quad \kappa_2 = \frac{\partial^2 w}{\partial x_2^2}, \quad \kappa_3 = \frac{\partial^2 w}{\partial x_1 \partial x_2}$$

substituting eq. (5.11) into the equation for the strain energy density of a single bond-pair,

$$\begin{aligned} w &= \omega(\xi)\alpha [1 + \cos(\theta(\underline{\mathbf{Y}}\langle\xi\rangle, \underline{\mathbf{Y}}\langle-\xi\rangle))] \\ &= \omega(\xi)\alpha \frac{\xi^2}{8} (\kappa_1^2 \cos^4(\phi) + \kappa_2^2 \sin^4(\phi) + 2\kappa_1\kappa_2 \cos^2(\phi) \sin^2(\phi) + 4\kappa_3^2 \cos^2(\phi) \sin^2(\phi) \\ &\quad + 4\kappa_1\kappa_3 \cos^3(\phi) \sin(\phi) + 4\kappa_2\kappa_3 \cos(\phi) \sin^3(\phi)) + \mathcal{O}(\xi^4). \end{aligned}$$

If we use a weighting function $\omega(\xi) = \omega(\xi)$ and assume that the ω plays the role of a localization kernel, i.e. $\omega = 0 \forall \xi > \delta$, the resulting strain energy density, W , for any material point in the peridynamic plate is

$$\begin{aligned} W &= \alpha \int_0^\delta \int_0^{2\pi} w \xi d\phi d\xi, \\ &= \alpha \frac{3\pi}{8} \left(\kappa_1^2 + \kappa_2^2 + \frac{2}{3}\kappa_1\kappa_1 + \frac{4}{3}\kappa_3^2 \right) \int_0^\delta \omega(\xi) \xi^3 d\xi + \mathcal{O}(\delta^6). \end{aligned}$$

Equating W with the classical Kirchhoff plate strain-energy density, Ω , and taking the limit as $\delta \rightarrow 0$ we can solve for α

$$\begin{aligned} \lim_{\delta \rightarrow 0} W &= \Omega, \\ \alpha \frac{3\pi}{8} m \left(\kappa_1^2 + \kappa_2^2 + \frac{2}{3}\kappa_1\kappa_1 + \frac{4}{3}\kappa_3^2 \right) &= \left[\frac{Gh^3}{12(1-\nu)} (\kappa_1^2 + \kappa_2^2 + 2\nu\kappa_1\kappa_1 + 2(1-\nu)\kappa_3^2) \right]_{\nu=1/3}, \\ \alpha &= \frac{2Gh^3}{3m}, \end{aligned} \tag{5.12}$$

with

$$m = \int_0^\delta \int_0^{2\pi} \omega(\xi) \xi^2 \xi d\phi d\xi,$$

where G is the shear modulus, h is the thickness of the plate, and we have evaluated the classical Kirchhoff strain-energy at a Poisson ratio of $1/3$ in order to solve for alpha as a constant. Because α is inversely proportional to m , the energy does not change with varying choices for ω and δ . It should be noted that the restriction $\nu = 1/3$ is the same imposed by the use of a bond based

peridynamic model for in-plane deformation of a 2D peridynamic plate. We will show an extension to this model that removes this restriction in Section 5.4.

5.3.2 Combining Bending and Extension Models

The bond-pair bending model does not resist in-plane stretching or shear deformation because these deformations preserve the angles between opposite bonds. If these behaviors are expected in combination with bending, a useful model must resist both in-plane and transverse deformations. To create a plate model that also resists these deformations, i.e. a flat shell, we combine the bond-pair model with a two-dimensional version of the original bond-based linearly-elastic peridynamic solid model from [62]. In this model, individual bonds act as springs resisting changes in length.

$$\underline{\mathbf{T}}\langle\xi\rangle = \beta (|\underline{\mathbf{Y}}\langle\xi\rangle| - |\xi|) \frac{\underline{\mathbf{Y}}\langle\xi\rangle}{|\underline{\mathbf{Y}}\langle\xi\rangle|} \quad (5.13)$$

By matching the energy of a 2D material in shear deformation, we can relate β to the shear modulus and thickness of the shell. Following the example of [64], we begin with a 2D material under pure in-plane shear. In Einstein notation, the strain energy of this material is

$$W_C = G h \epsilon_{ij}^d \epsilon_{ij}^d,$$

$$\begin{aligned} W_{PD} &= \frac{\beta}{2} \int_A \omega(\xi) (|\underline{\mathbf{Y}}\langle\xi\rangle| - |\xi|)^2 dA_\xi, \\ &= \frac{\beta}{2} \int_A \omega(\xi) \frac{\epsilon_{ij}\xi_i\xi_j}{|\xi|} \frac{\epsilon_{kl}\xi_k\xi_l}{|\xi|} dA_\xi, \\ &= \frac{\beta}{2} \epsilon_{ij}^d \epsilon_{kl}^d \int_A \frac{\omega(\xi)}{|\xi|^2} \xi_i \xi_j \xi_k \xi_l dA_\xi. \end{aligned}$$

where ϵ^d is the deviatoric strain tensor. Now, to evaluate the integral we will exploit the symmetry properties. With $i, j, k, l = 1, 2$. For a circular $\omega(\xi) = \omega(|\xi|)$, combinations of $\{i, j, k, l\}$ with an odd number of each index, such as $\{1, 1, 1, 2\}$ or $\{2, 1, 2, 2\}$, will result in odd powers of sine and

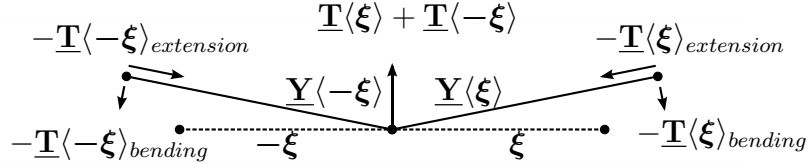


Figure 5.9: The Hybrid Model Combines Bending and Extension Components

cosine and integrate to 0.

$$\begin{aligned}
 m &= \int_A \omega(\xi) |\xi|^2 dA_\xi \\
 W_{\text{PD}}^d &= \frac{\beta m}{16} [3(\epsilon_{11}\epsilon_{11} + \epsilon_{22}\epsilon_{22}) + (\epsilon_{11}\epsilon_{22} + \epsilon_{12}\epsilon_{12} + \epsilon_{12}\epsilon_{21} + \epsilon_{21}\epsilon_{12} + \epsilon_{21}\epsilon_{21} + \epsilon_{22}\epsilon_{11})] \\
 &= \frac{\beta m}{16} \epsilon_{ij}^d \epsilon_{kl}^d (\delta_{ij}\delta_{kl} + \delta_{ik}\delta_{jl} + \delta_{il}\delta_{jk}) \\
 &= \frac{\beta m}{8} \epsilon_{ij}^d \epsilon_{ij}^d \implies \\
 \beta &= \frac{8 G h}{m}
 \end{aligned}$$

Having calibrated the bond-extension model to the shear modulus for a case of pure in-plane shear, applying a different uniform strain (such as might result from uniaxial tension) reveals the bond-based model to result in a one-parameter linearly-elastic model with Poisson's ratio $\nu = 1/3$.

Combining the bending and extension models allows for the description of more complex behaviors, particularly the stiffening effect of in-plane tension on the transverse bending of a shell. Consider a single bond-pair in the combined model shown in Fig. 5.9. As the two sides are pulled apart, the magnitude of the extension force in each bond increases, and the magnitude of the bending force decreases. At the same time, the angle at which the extension force acts decreases, and the angle of action for the bending force increases. For small amounts of bending and reasonable stretches, increased tension in the direction of the bond pair results in increased restorative force.

5.4 Extension to arbitrary Poisson ratio

Although many materials have Poisson ratios of $\nu \approx 1/3$, it is nonetheless desirable to extend the model to materials with arbitrary Poisson ratios. For isotropic, linearly elastic models of solid materials, Silling et al. extended the peridynamic material model to arbitrary material parameters in [64] by decomposing the deformation into isotropic and deviatoric components. In the absence of plastic deformation, we need only find the difference between the strain energy of a deformed bond-based plate and the strain energy of an elastic plate with Poisson's ratio $\nu \neq 1/3$. The difference is a function of the isotropic strain in two dimensions, θ_2

$$\begin{aligned} W' &= \frac{G h}{2} \left(\frac{3\nu - 1}{1 - \nu} \right) \theta_2^2 \\ \theta_2 &= \frac{2}{m} \int_A \omega(\boldsymbol{\xi}) |\boldsymbol{\xi}| (|\underline{\mathbf{Y}}(\boldsymbol{\xi})| - |\boldsymbol{\xi}|) dA_{\boldsymbol{\xi}} \\ W_{\text{total}} &= \frac{G h}{2} \left(\frac{3\nu - 1}{1 - \nu} \right) \theta_2^2 + \frac{4 G h}{m} \int_A \omega(\boldsymbol{\xi}) (|\underline{\mathbf{Y}}(\boldsymbol{\xi})| - |\boldsymbol{\xi}|)^2 dA_{\boldsymbol{\xi}} \end{aligned}$$

This is to be expected because the bond-based model was calibrated to the shear strain energy, leaving discrepancies proportional to the isotropic strain energy that fall to 0 as Poisson's ratio approaches $\nu = 1/3$.

This decomposition method inspires a similar approach to our plate model. To perform the same extension for the plate model in bending, we find the error in the 1-parameter strain energy for $\nu \neq 1/3$

$$\begin{aligned} W' &= \frac{Gh^3}{12(1-\nu)} (\kappa_1^2 + \kappa_2^2 + 2\nu\kappa_1\kappa_2 + 2(1-\nu)\kappa_3^2) \\ &\quad - \frac{Gh^3}{12(1-\frac{1}{3})} \left(\kappa_1^2 + \kappa_2^2 + \frac{2}{3}\nu\kappa_1\kappa_2 + 2(1-\frac{1}{3})\kappa_3^2 \right) \\ W' &= 2G \frac{h^3}{12} \frac{3\nu - 1}{1 - \nu} \left(\frac{\kappa_1 + \kappa_2}{2} \right)^2. \end{aligned}$$

The discrepancy in energy is proportional to the square of average curvature, $\frac{\kappa_1 + \kappa_2}{2} = \bar{\kappa}$, which we will also refer to as the isotropic curvature. The isotropic curvature can be envisioned as the

portion of the deformation that resembles a hemispherical bowl. The remainder of the bending deformation, that which is left when the isotropic curvature is subtracted out, resembles a saddle. This remaining component is the deviatoric deformation, and both components are shown in fig. 5.10. Note that the orientation of the deviatoric bending will change depending on the particular curvature being decomposed, while the isotropic curvature will only change in scale. A

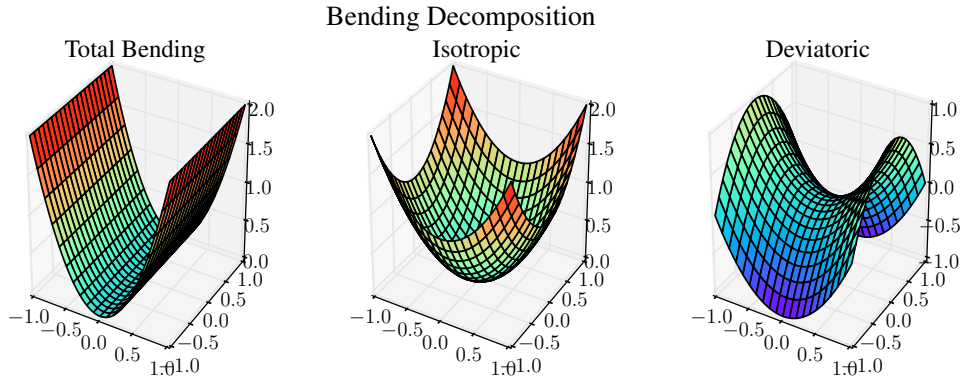


Figure 5.10: Bending Deformation Decomposed into Isotropic and Deviatoric Portions

complete decomposition of bending energy into isotropic and deviatoric components as performed by Fischer in [24] produces a far more complex model and is unnecessary at this time. For a single bond pair we can represent the curvature vector along the bond pair as

$$\kappa_{\xi} = \frac{\underline{Y}\langle\xi\rangle + \underline{Y}\langle-\xi\rangle}{|\xi|^2}$$

For large rotations, we can define an average curvature vector $\bar{\kappa}$. This leads us to model the average curvature as

$$\begin{aligned}\bar{\kappa} &= \frac{1}{m} \int_0^\delta \int_0^{2\pi} \omega(\xi) \frac{\underline{Y}\langle\xi\rangle + \underline{Y}\langle-\xi\rangle}{\xi^2} \xi d\phi d\xi; \\ m &= \int_0^\delta \int_0^{2\pi} \omega(\xi) \xi d\phi d\xi.\end{aligned}$$

The weighting function $\omega(\xi)$ performs the same function as in the previous section. We can rewrite

the energy discrepancy in terms of $\bar{\kappa}$.

$$W' = 2G \frac{h^3}{12} \frac{3\nu - 1}{1 - \nu} \bar{\kappa}^2.$$

We can take the Fréchet derivative (details in A) to produce a correction force vector state

$$\underline{\mathbf{T}}' \langle \xi \rangle = \frac{8G}{m} \frac{h^3}{12} \frac{3\nu - 1}{1 - \nu} \frac{\omega(\xi)}{\xi^2} \bar{\kappa}, \quad (5.14)$$

that is not directly dependent on the deformation of a single bond pair. Instead, eq. (5.14) represents a bond-length dependent “pressure” applied to every pair of bonds extending from a node. This “pressure” is proportional to the curvature vector at that node. A weighting function $\omega(\xi) = |\xi|$ can ensure that the integral expression for force at a point is convergent. This extra term that is dependent on the bending of all the pairs around a material point means that the extension is not properly a *bond-pair* model. Instead, it would be more accurate to call it a *bond-multiple* model, in which the bond forces and energies are functions of the relationship between a family of bonds. In either the continuous or discrete cases, this model extension requires the additional step of evaluating the isotropic curvature at each point, but the increased complexity of the extended model captures in the local limit the behavior of a two-parameter elastic material plate.

Chapter 6: NUMERICAL SIMULATION

6.1 Discretized Bond Pair Beam

Discretizing the bond-pair model is primarily matter of exchanging integrals for sums.

$$\begin{aligned} w(\boldsymbol{\xi}_i) &= \omega(\boldsymbol{\xi}_i) \alpha [1 + \cos(\theta(\underline{\mathbf{Y}}\langle\boldsymbol{\xi}_i\rangle, \underline{\mathbf{Y}}\langle-\boldsymbol{\xi}_i\rangle))] \\ &\approx \omega(\boldsymbol{\xi}_i) \frac{\alpha}{2} \left(\frac{v(\mathbf{x} + \boldsymbol{\xi}_i) - 2v(\mathbf{x}) + v(\mathbf{x} - \boldsymbol{\xi}_i)}{\boldsymbol{\xi}_i} \right)^2 \end{aligned}$$

in which $\boldsymbol{\xi}_i$ is the i^{th} bond emanating from the point \mathbf{x} to each of the n points within distance δ of point \mathbf{x} .

$$\begin{aligned} \alpha &= \frac{c \Delta x}{m}; \quad c = EI; \quad m = \sum_{i=1}^n \omega(\boldsymbol{\xi}_i) \boldsymbol{\xi}_i^2 \implies \\ W &= \Delta x \sum_{i=1}^n \frac{EI}{2} \omega(\boldsymbol{\xi}_i) \left(\frac{v(\mathbf{x} + \boldsymbol{\xi}_i) - 2v(\mathbf{x}) + v(\mathbf{x} - \boldsymbol{\xi}_i)}{\boldsymbol{\xi}_i} \right)^2 \end{aligned}$$

Discretization of the original model results in the equation of motion

$$\begin{aligned} \rho(\mathbf{x}) \ddot{\mathbf{u}}(\mathbf{x}) &= \mathbf{f}(\mathbf{x}) + \sum_i \omega(\boldsymbol{\xi}_i) \left\{ \frac{\alpha(\mathbf{x})}{|\mathbf{p}_i|} \frac{\mathbf{p}_i}{|\mathbf{p}_i|} \times \left[\frac{\mathbf{p}_i}{|\mathbf{p}_i|} \times \frac{\mathbf{q}_i}{|\mathbf{q}_i|} \right] \right. \\ &\quad \left. - \frac{\alpha(\mathbf{x} + \boldsymbol{\xi}_i)}{|\mathbf{p}_i|} \frac{(-\mathbf{p}_i)}{|\mathbf{p}_i|} \times \left[\frac{(-\mathbf{p}_i)}{|\mathbf{p}_i|} \times \frac{\mathbf{r}_i}{|\mathbf{r}_i|} \right] \right\} \end{aligned} \quad (6.1)$$

with

$$\mathbf{p}_i = \boldsymbol{\xi}_i + \mathbf{u}(\mathbf{x} + \boldsymbol{\xi}_i) - \mathbf{u}(\mathbf{x});$$

$$\mathbf{q}_i = -\boldsymbol{\xi}_i + \mathbf{u}(\mathbf{x} - \boldsymbol{\xi}_i) - \mathbf{u}(\mathbf{x});$$

$$\mathbf{r}_i = \boldsymbol{\xi}_i + \mathbf{u}(\mathbf{x} + 2\boldsymbol{\xi}_i) - \mathbf{u}(\mathbf{x} + \boldsymbol{\xi}_i).$$

and for small displacements and rotations in a uniform beam,

$$\rho(\mathbf{x})\ddot{v}(\mathbf{x}) = f(\mathbf{x}) + \alpha \sum_i 2\omega(\xi_i) \left(\frac{v(\mathbf{x} - 2\xi_i) - 4v(\mathbf{x} - \xi_i) + 6v(\mathbf{x}) - 4v(\mathbf{x} + \xi_i) + v(\mathbf{x} + 2\xi_i)}{\xi_i^2} \right)$$

It is worth noting the similarity between this expression and a finite-difference fourth derivative of displacement, a result expected from Euler beam theory. This discretization requires that nodes be evenly spaced along the entire beam, otherwise the displacement $v(\mathbf{x} - \xi_i)$ is ill-defined. For this reason, the discretization does not allow for areas of higher and lower “resolution”.

6.2 Discretized Bond Pair Plate

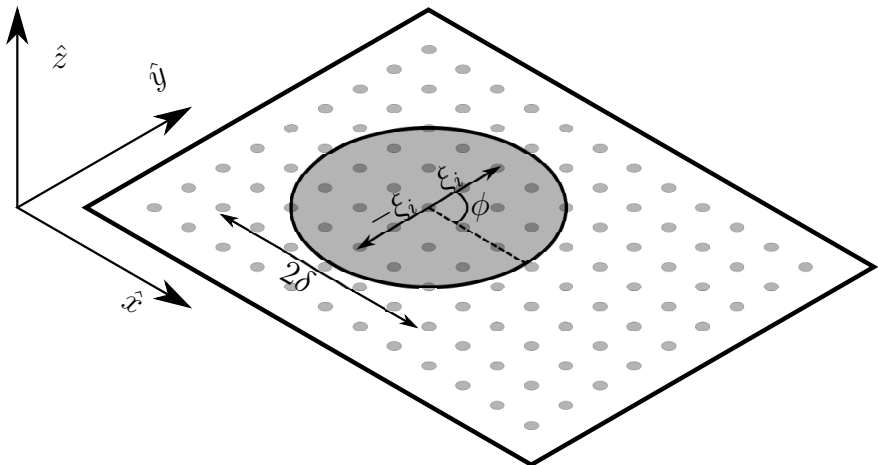


Figure 6.1: Discretized peridynamic plate with illustrated bond pair

As with the beam, discretizing the bond-pair model is primarily matter of exchanging integrals

for sums.

$$\alpha = \frac{c (\Delta x)^2}{m}; \quad c = \frac{G}{(1-\nu)} \frac{h^3}{12}; \quad m = \sum_{i=1}^n \omega(\xi_i) \xi_i^2 \implies \\ W = (\Delta x)^2 \sum_{i=1}^n \omega(\xi_i) \frac{G}{2(1-\nu)} \frac{h^3}{12} \left(\frac{w(\mathbf{x} + \xi_i) - 2w(\mathbf{x}) + w(\mathbf{x} - \xi_i)}{|\xi_i|} \right)^2$$

Discretization of the 1-parameter bending model results in the same equation of motion as for the beam model (eq. 6.1).

Implementing the 2-parameter model requires finding the isotropic curvature at each point.

$$\bar{\kappa}(\mathbf{x}) = \frac{1}{m} \sum_i \omega(\xi_i) \frac{\mathbf{p}_i + \mathbf{q}_i}{\xi_i^2}; \\ m(\mathbf{x}) = \sum_i \omega(\xi_i); \\ \alpha^{\text{iso}}(\mathbf{x}) = \frac{4G}{m} \frac{h^3}{12} \frac{3\nu - 1}{1 - \nu} (\Delta x)^2; \\ f^{\text{iso}}(\mathbf{x}) = \sum_j \left\{ [\alpha^{\text{iso}}(\mathbf{x}) \bar{\kappa}(\mathbf{x}) - \alpha^{\text{iso}}(\mathbf{x} + \xi_j) \bar{\kappa}(\mathbf{x} + \xi_j)] \frac{\omega(\xi_j)}{\xi_j^2} \right\}$$

As with the discretized beam, the discretization of the bond-pair plate (fig. 6.1) must be absolutely regular. Discretizing the bond-pair model as proposed above requires that nodes be evenly spaced, Δx , throughout the entire plate, otherwise the displacement $w(\mathbf{x} - \xi_i)$ is undefined. For this reason, the discretization does not allow for areas of higher and lower “resolution”. This restriction, while inconvenient in the 1D case, is fairly restricting for plate analysis. An extension to this discretization that would allow changing mesh resolution will require interpolation between the nodes.

6.2.1 Curved Shapes

On a curved surface, the location of the point $\mathbf{x} - \xi$ might be off of the surface entirely. One method of applying the bond-pair model to curved surfaces is through the use of “virtual” points. These points have no mass and do not have families of peridynamic neighbors, they only allow the

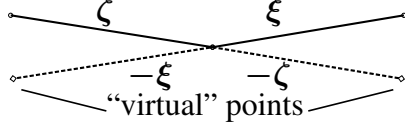


Figure 6.2: Virtual Points Allow Straight Pairs on Curved Surfaces

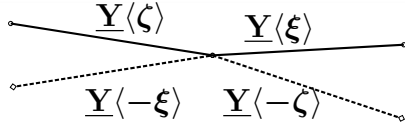


Figure 6.3: Virtual Points Take the Displacement of Nearby Real Points

definition of bond pairs that are straight in the undeformed configuration. In the simplest method, each virtual point is located just above or below a real point in the model. In this case, properties such as displacement are taken to be the same as for the nearby real point. Because the virtual point has no mass is not part of any other bond pairs, it cannot be assigned a force. Instead, the force on a virtual point resulting from deformation of a bond pair is instead applied to the nearest real points. This results in a straightforward extension of the bending model from flat plates (and beams) to features that have curvatures that are small over the peridynamic horizon.

6.2.2 Irregular Discretization

A curved surface is not the only reason to implement virtual points, and even many curved surfaces do not allow for regular discretization. When discretization is irregular, due to three-dimensional curvature, irregular shapes, or a need for increased resolution in some areas, there are necessarily points at which there is no real point at the location of $x - \xi$. An example of changing mesh density resulting in a need for interpolation can be found in fig. 6.4, which shows a small family of nodes at the edge of a change in discretization coarseness. Note that, while bonds p_2 and q_2 form a perfect bond pair, there is no bond exactly opposite p_1 . To solve this, we add a virtual point to create a bond, q_1 , that will form a pair with p_1 . Because this point is not part of the

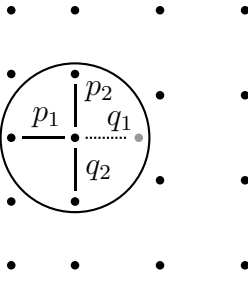


Figure 6.4: Virtual Points Pair Up Unpaired Neighbors

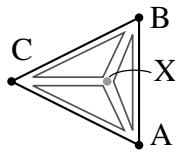


Figure 6.5: Barycentric interpolation is based on the relative areas of sub triangles

discretization, it has no mass, and its properties must be determined from the properties of the surrounding nodes. An easy method of determining properties (such as displacement) at virtual nodes is to use a weighted average. One method of generating useful weights that is relatively robust is barycentric interpolation. We start by finding the three (non-collinear) real nodes closest to the location of the virtual node, A, B, and C. Next, we find the signed areas of the triangles ABC, ABX, BCX, and CAX, with X being the virtual node. The weight of node A is the area ratio between BCX and ABC, the weight of node B is the ratio of areas CAX and ABC, and the weight of node C is the ratio of areas ABX to ABC. Using signed areas allows the weights to be negative to extrapolate properties of a virtual node outside of ABC. Because these weights are calculated from the initial positions of the node, they can be stored for swift evaluation of properties at virtual nodes.

With the properties of the virtual points determined, the model can be evaluated in the same manner as the uniformly discretized models of the previous papers. Where forces are calculated to act on a virtual node, those forces are redistributed to the supporting real nodes according to the weight each point has in the interpolation.

The same method of virtual nodes also allows the modeling of curved surfaces, in which the perfect opposite of a bond may not lie near but not on the surface of the plate or shell. As long as the curvature of the surface is small (at the scale of the peridynamic horizon), each resulting virtual nodes will be nearly in the plane formed by its nearest neighbors. Finding the weights of the surrounding nodes is performed just as in the planar case, except that the areas are formed between the projection of the virtual node location X onto the plane formed by A, B, and C.

To compute the weight of node A in the interpolation of properties at virtual node X, let AB represent the vector from node A to node B, and use

$$W'_A = \frac{B - X}{2} \bullet \left[BC \times \left(\frac{BC \times BA}{|BC \times BA|} \right) \right] \quad (6.2)$$

After finding W'_B and W'_C in similar fashion,

$$W_A = \frac{W'_A}{W'_A + W'_B + W'_C} \quad (6.3)$$

If the projection of X onto the plane defined by A, B, and C lies outside the triangle ABC, one or two of W_A , W_B and W_C will be negative, though they will still sum to 1.

6.3 “Boundary” Conditions

Because peridynamic models result in long range forces, it is not sufficient to apply boundary conditions to nodes on the relevant boundary; nodes near the boundary must be considered as well. For the peridynamic beam we consider applied forces, simple supports or rollers, and fixed or clamped supports. Simply-supported beams are easy to model because only displacement is constrained. To add a roller support to the peridynamic beam, it suffices to constrain the movement of the nearest peridynamic node in the appropriate degree(s) of freedom. Simulating a “clamped” end condition is a little less intuitive. The most basic way to simulate a clamped end is to extend the beam 2δ , or twice the horizon, into the clamp. The displacement of all of those nodes is set

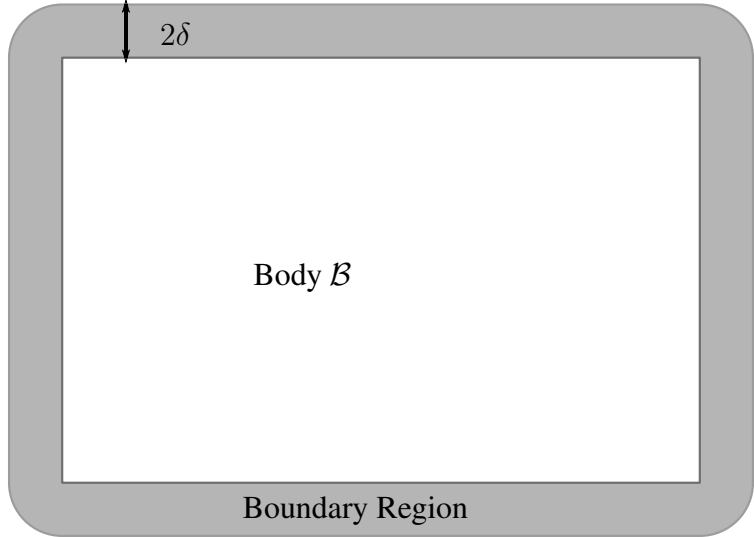


Figure 6.6: The boundary of a peridynamic model is a region of nonzero thickness

to zero, or whatever value is appropriate for a displaced or rotated clamp. In classical mechanics, a clamped end can be described with a symmetry condition, but the two are not peridynamically equivalent. Because the classical beam is a local model, material at a clamp cannot “see” distant material, so there is no way to distinguish between a beam end that is clamped and one that is bent symmetrically over an appropriate sawhorse. Distributed forces may be applied as expected to nodes in the loaded region. Point forces may often be applied directly to the nearest node, or to the nodes immediately surrounding the point of application. Point moments must also be considered more carefully because the peridynamic models in this work, like most peridynamic models, do not consider rotational degrees of freedom for peridynamic nodes. Rather, material rotation is the result of the relative translational displacement of multiple nodes. It is therefore impossible to apply a moment to a single peridynamic point. Instead, moments may be applied as force couples to the bonds attached to the peridynamic node nearest the location of the desired moment. For example, if we want to apply a moment M at point \mathbf{x} , whose n neighboring points \mathbf{x}'_i are connected to \mathbf{x} in the undeformed configuration by bonds ξ_i . For an evenly discretized beam,

we may distribute the moments by

$$\mathbf{M}_i = \mathbf{M} \frac{\omega(\xi_i)}{\sum_{j=1}^n \omega(\xi_j)}$$

and apply them to the corresponding bonds by adding forces

$$\mathbf{F}_i = \mathbf{M}_i \times \frac{\mathbf{Y}\langle\xi_i\rangle}{|\mathbf{Y}\langle\xi_i\rangle|^2}$$

to each point \mathbf{x}_i and subtracting them from the force at \mathbf{x} .

Support configurations are similar for two-dimensional models. Each node along a simply-supported edge is constrained in one or more directions. As with the beam model, clamped edges are implemented by extending the surface into the clamp. Line and pressure loads are treated normally.

6.4 Numerical Solution Method

This project uses Trilinos, a collection of open software libraries, or packages, from Sandia National Labs, including:

- Epetra and EpetraExt - provide efficient parallel data structures, particularly vectors and sparse matrices
- Isorropia - provides load balancing, partitioning, and matrix coloring
- NOX - a collection of large-scale nonlinear system solver utilities
- PyTrilinos - a python interface providing Python wrappers for many Trilinos packages, and offering compatibility between numpy.ndarrays and Epetra.MultiVectors

The nature of discrete peridynamic models results in large numbers of parallelizable computations. Efficient parallelization is achieved using Epetra data structures for distributed variables.

Model force evaluations are coded in Python, making extensive use of the optimized routines in the NumPy and SciPy packages operating on the distributed Epetra objects. To obtain quasistatic solutions, problems are coded into NOX objects and solved using NOX nonlinear solvers. Preliminary analysis was performed using a Newton Method solver on an iMac with a 3.1GHz Intel Core i7 processor and 16GB RAM, using 1-4 cores. Later work also performed on Shamu, a High-Performance Computing cluster at UTSA. The nature of the Trilinos packages and the structure of the code allow for more extensive parallel computation without major code changes.

For all but the simplest loading conditions, analytical solutions to boundary condition problems become complicated. As load conditions and material behavior become more complex, there are no analytical solutions. For comparison, equivalent models are created and analyzed in Abaqus 6.12 to verify simple cases.

6.5 Results

6.5.1 Straight Beam Results

The simplest test case for this model is a linear-elastic beam with a square profile. For comparison, equivalent models are created and analyzed in Abaqus 6.12 to verify simple cases. Even a coarse discretization successfully reproduces the shape of the elastically deformed, simply-supported beam shown in fig. 6.7. It is more difficult to accurately reproduce the behavior of a clamped-

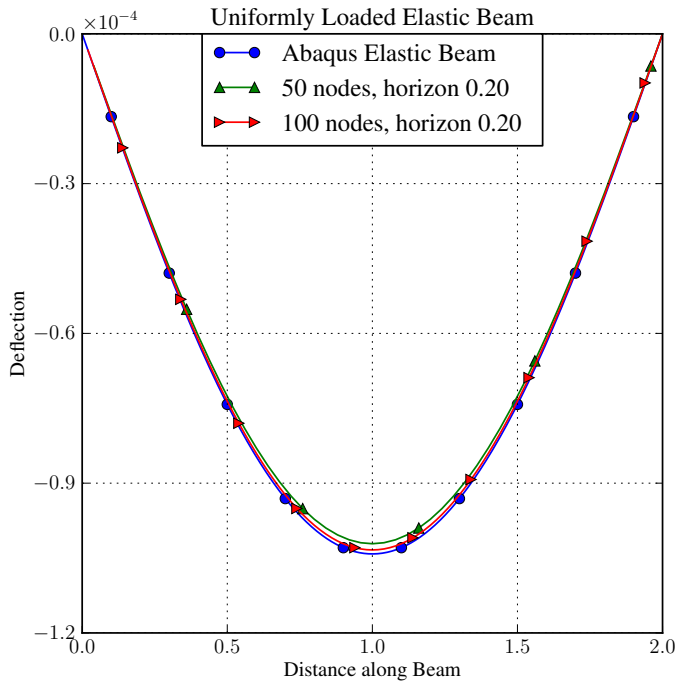


Figure 6.7: The uniform-load elastic beam is accurately modeled with few nodes

end beam. It is evident from figs. 6.8 and 6.9 that the clamped end constraint requires far more nodes and a smaller horizon to reproduce the results of a classical elastic model.

As an elastic-perfectly-plastic beam exceeds the elastic limit of its material, plastic zones begin to grow on the top and bottom of the beam's cross section. This behavior is mimicked by the plasticity of the longest bond-pairs described in eq. (5.8), producing the results shown in fig. 6.10. To accurately capture this phenomenon and model beam plasticity, a finer discretization is required.

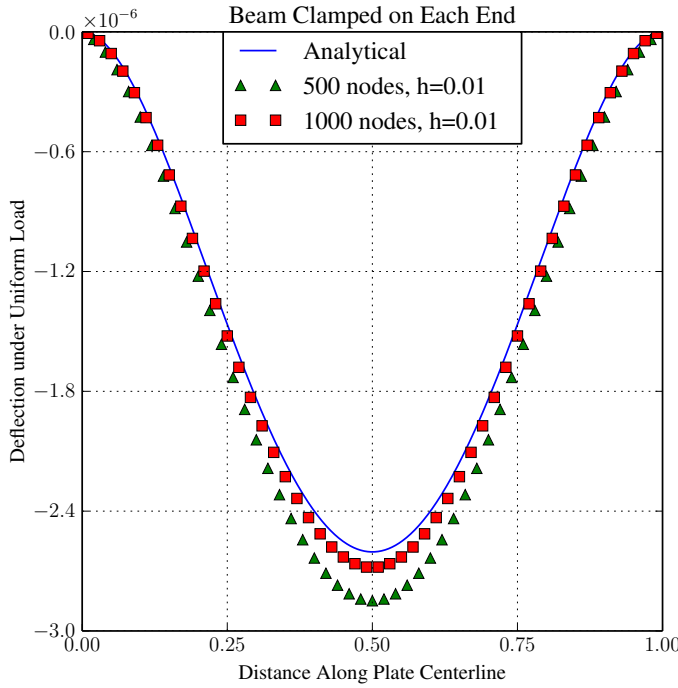


Figure 6.8: The clamped condition requires finer discretization

A material that is plastically deformed does not return to its original state when unloaded. For a beam in bending, the residual deformations can be seen in a beam that has been loaded beyond the onset of plastic deformation and then unloaded. The Abaqus model retains slightly more than $\frac{1}{10}$ of its loaded displacement after being completely unloaded. This result is observed in the bond-pair plasticity model, shown in figs. 6.11 and 6.12. Accurate residual deformation modeling requires both a relatively small horizon and a fairly large number of nodes.

It is more difficult to verify the brittle material model described by eq. (5.9) because brittle failure is unstable. When a crack begins, moment is transferred to other bond pairs, and failure progresses until every pair of bonds surrounding a node are broken, creating a hinge at that node. This is borne out by the results in fig. 6.13, in which “Nodal Health” represents the fraction of bond-pairs about each node that have never exceeded their critical angle and therefore have not failed.

Unlike a local model, partial failure is observed at nodes near the plastic hinge, as pairs of

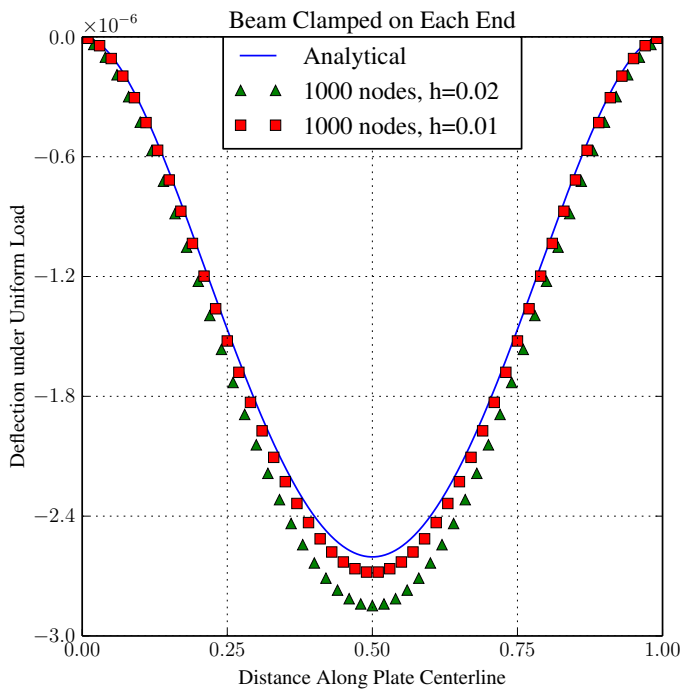


Figure 6.9: The clamped condition requires a smaller horizon

bonds that straddle the hinge are broken.

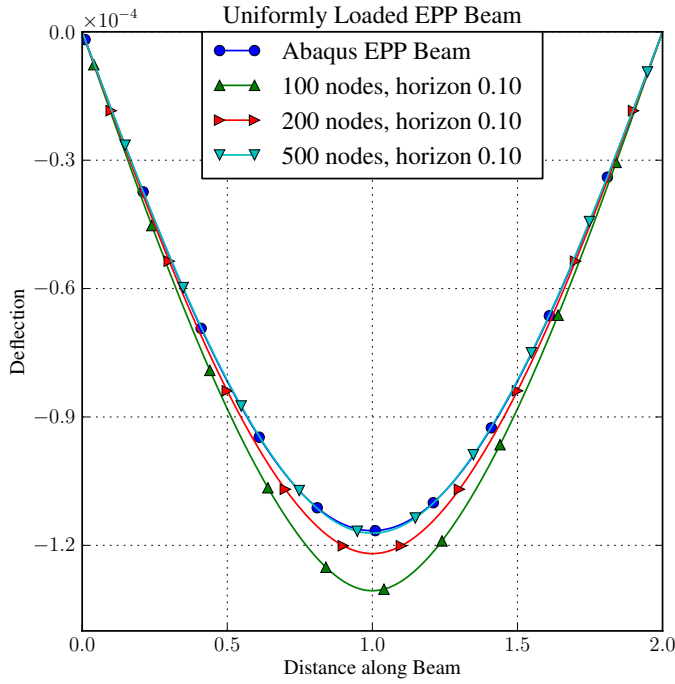


Figure 6.10: The elastic perfectly-plastic beam requires finer discretization

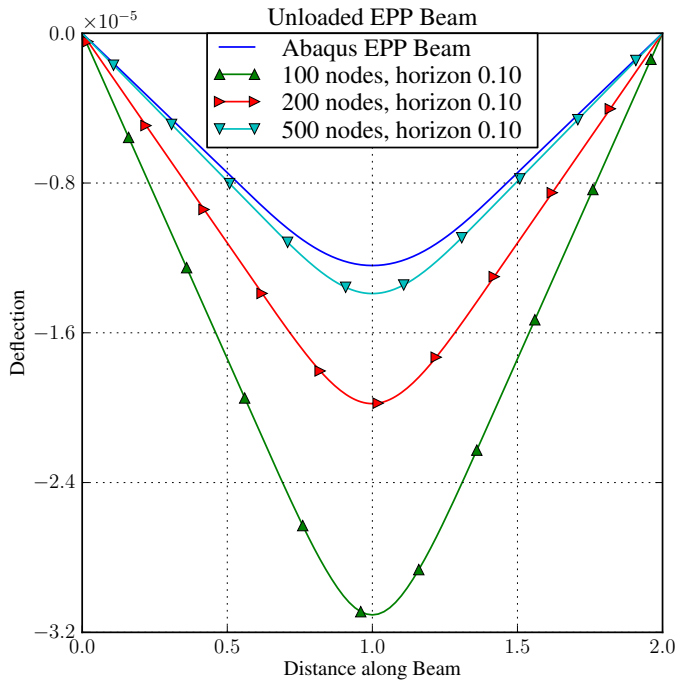


Figure 6.11: The need for fine discretization is even more apparent when representing residual plastic deformation

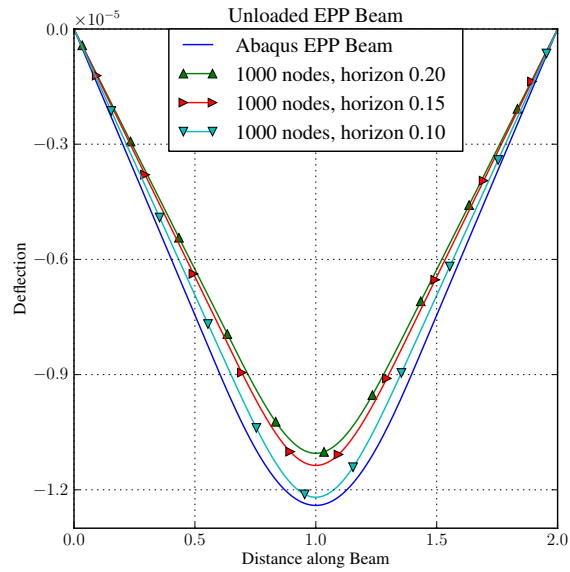


Figure 6.12: Accurately modeling residual plastic deformation also requires a small horizon

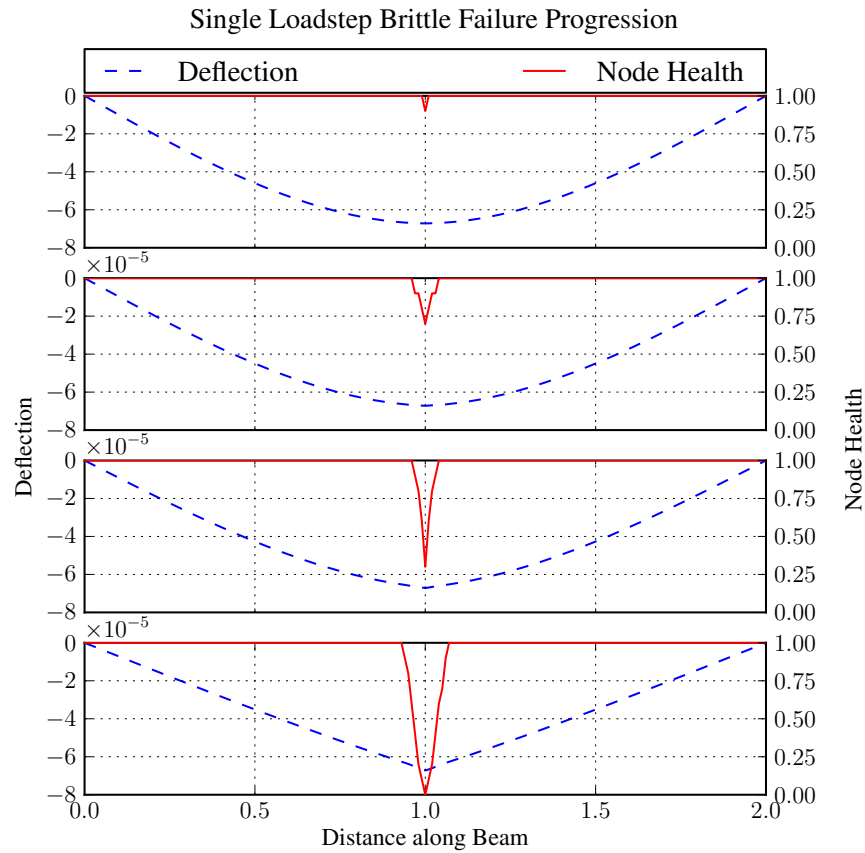


Figure 6.13: A brittle beam with prescribed center displacement

6.5.2 Flat Plate Results

The simplest test case for the 2D model is a linear-elastic square plate with Poisson's ratio $\nu = 1/3$ that is simply-supported on all 4 sides with a uniform transverse pressure load on the entire surface between the supports. As expected from an energy-equivalent model, the slice along the plate's centerline shown in fig. 6.14 demonstrates good agreement between the static deflection predicted by the bond-pair model and that of classical linear elasticity as the horizon length shrinks. This convergence only continues to a minimum horizon, below which the discretized equation of motion (eq. (6.1)) ceases to accurately approximate the continuous integral formulation (eqs. (4.1) and (5.1)). The minimum horizon size depends on the discretization; it appears that three times the node spacing is sufficient, but that a horizon that is only twice the node spacing is insufficient. The difference is evident in fig. 6.15, which also shows that results are insensitive to fineness of discretization once the minimum horizon criterion is met. Accurate results require a denser

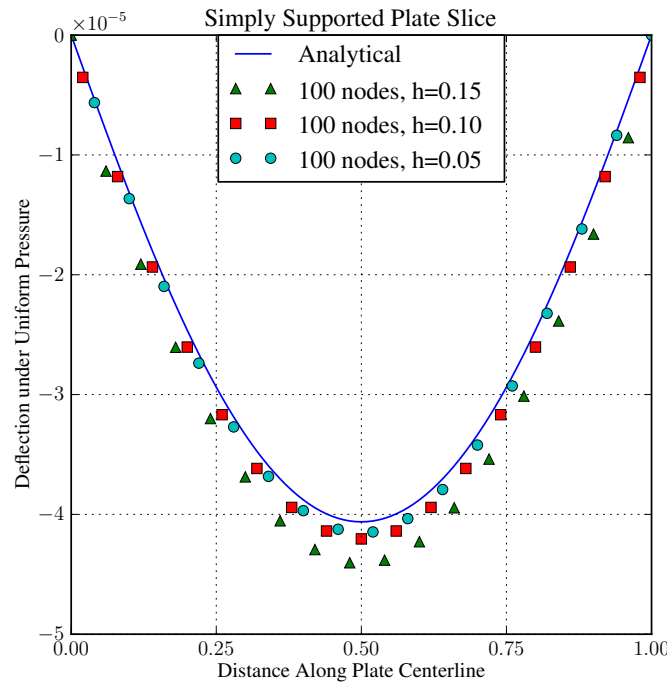


Figure 6.14: The Bond-Pair Model Converges on Accurate Plate Deflection with Smaller Horizons

discretization than is the case for the elastic beams from previous work. Figure 6.16 illustrates

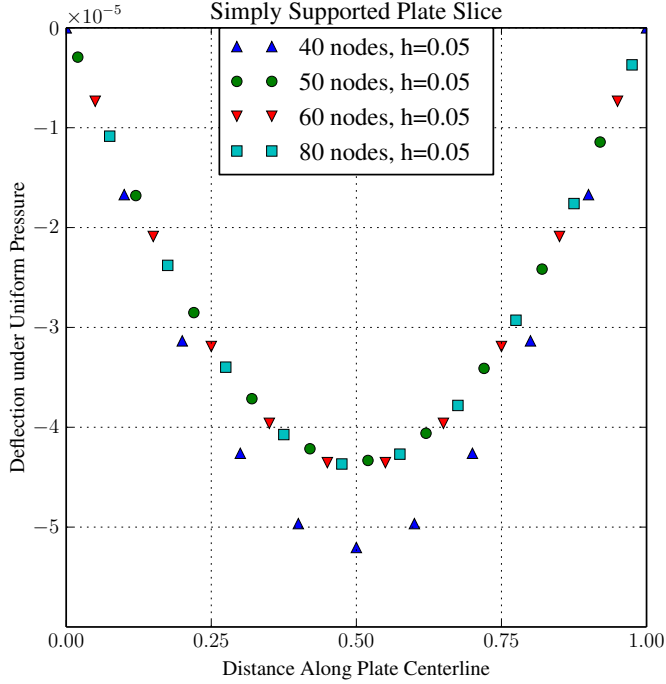


Figure 6.15: Horizon Must Include Sufficient Nodes

the model converging to the analytical solution as the discretization is made finer and the horizon shrinks.

The test case for the hybrid model is a similar simply-supported square plate with an additional in-plane tension load along two opposing sides. An analytical solution for this combination of uniform transverse pressure and in-plane edge tension can be found in Timoshenko's book [72]. As is mechanically intuitive, increasing in-plane tension results in decreasing transverse displacement, while the opposite is true for compressive edge loading. Normalized to the maximum displacement of a transversely-loaded plate with no in-plane edge loads, the results in fig. 6.17 show that the hybrid model does a good job of simulating the impact of in-plane tension on maximum transverse deflection. The bond-multiple plate model is motivated by the desire to extend the bending model to an arbitrary Poisson's ratio, so the obvious test for this model is the same as for the bond-pair model. When compared to analytical predictions, fig. 6.18 demonstrates the bond-multiple model's ability to simulate plates with Poisson's ratios that depart significantly from

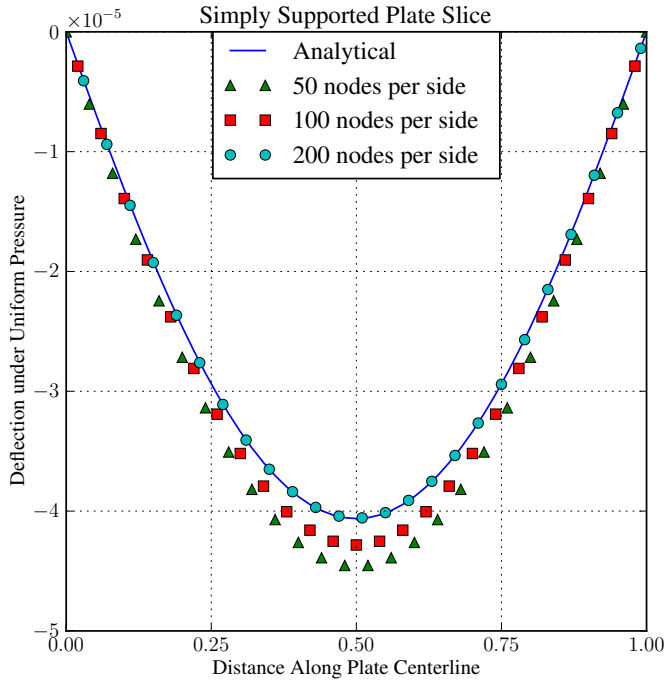


Figure 6.16: The Bond-Pair Model Converges on Accurate Plate Deflection with Finer Discretization

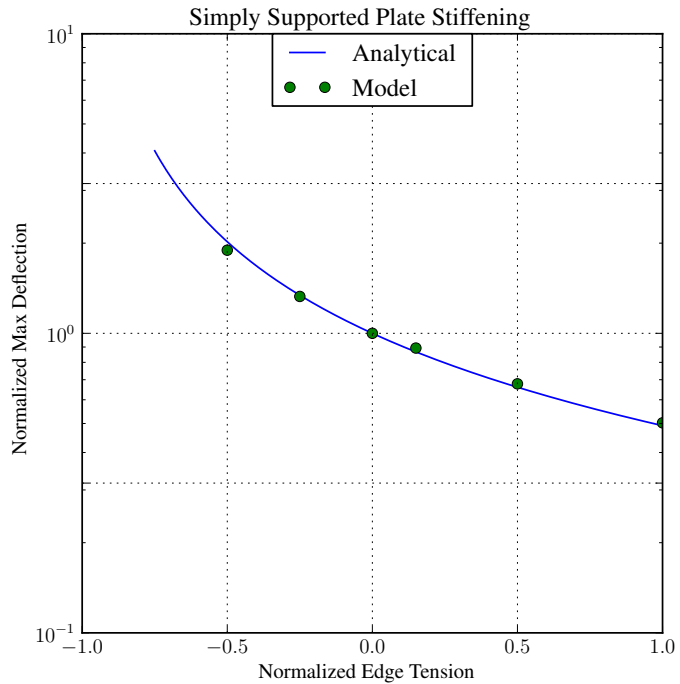


Figure 6.17: The Combined Model Accurately Captures the Influence of In-Plane Tension

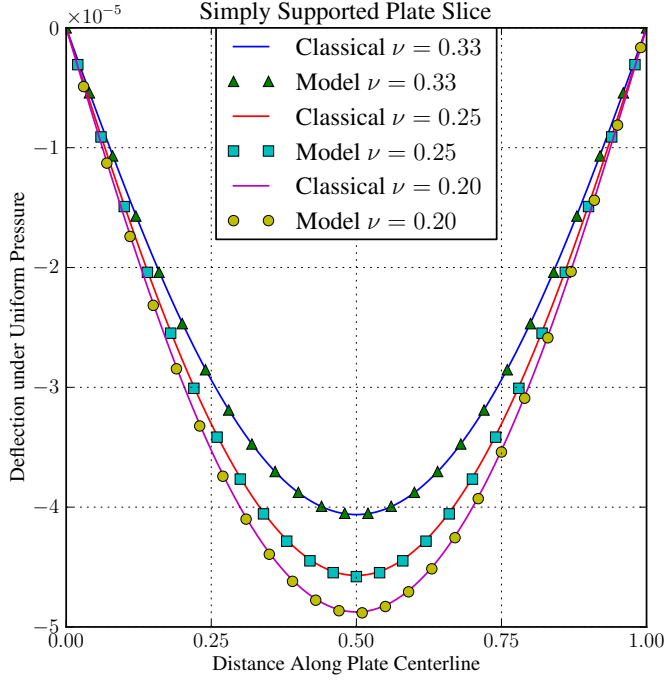


Figure 6.18: The Extended Model Matches for Arbitrary Poisson’s Ratio

the bond-pair limitation of $\nu = 1/3$.

Unlike the brittle beam, failure in a brittle plate need not progress unstably. To demonstrate the behavior of this model, a controlled-displacement double-torsion fracture test was simulated with the bond-pair model. A good review of the double-torsion test is available in [61]. The simple qualitative results are shown in fig. 6.19, colored by the fraction of failed bond pairs around each node. For each successive displacement load, the stable progression of the damaged region extends further into the plate. As with the brittle beam, the region within one horizon of the crack shows partial damage. In the double-torsion plate, the crack is expected to progress straight across the plate. A more interesting failure pattern can be found if the displacement is applied to only one of the two sides of the pre-crack. In a “single torsion” cracked plate, the crack path is expected to curve, and this result can be seen in fig. 6.20.

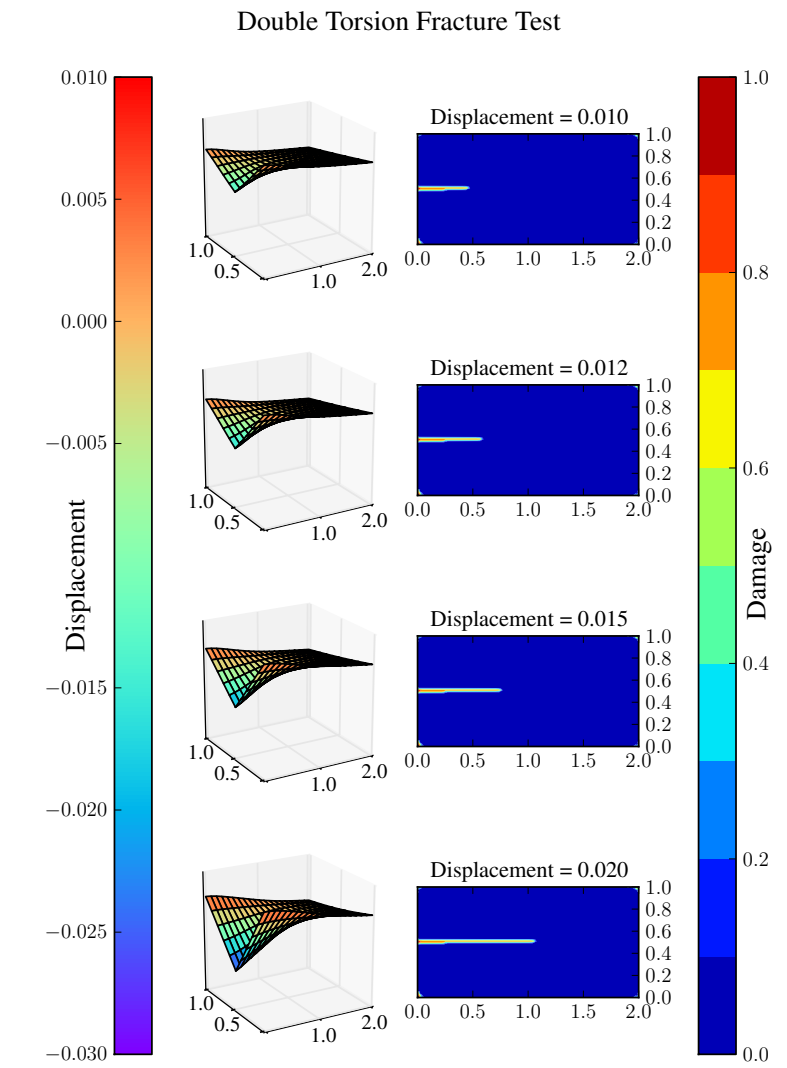


Figure 6.19: Crack Progression in Double Torsion Brittle Plate

Single Torsion Fracture

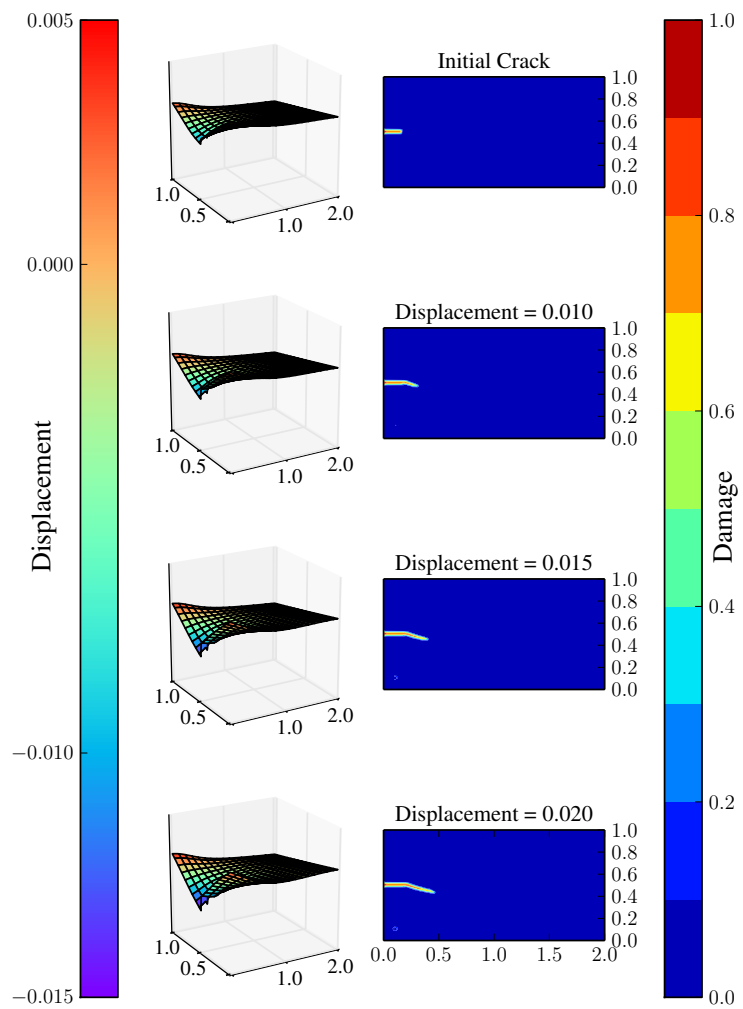


Figure 6.20: Crack Progression in Single Torsion Brittle Plate

Chapter 7: CONCLUSION

As far as we know, these are the first peridynamic state-based thin feature models.

The models developed so far provide allow for peridynamic modeling of peridynamic beams and plates in elastic bending. The models are validated by comparing their strain energies to the strain energy of classical models for small, homogenous deformations. Code was written to evaluate both beam and plate bond-pair models for linear elastic, brittle, nonlinear elastic, and elastic perfectly plastic materials. Simulations run with the developed models provide results in agreement with conventional methods for simple cantilever beam tests. Plate simulation results are promising but not yet verified for either elastic or elastic perfectly plastic materials. The proposed damage model successfully reproduces the impact of nonlinear elasticity on deformation of a rectangular cantilever, and the framework is laid to allow application of the same model to plates and I-beams. Plastic deformation results for rectangular cantilevers are promising, but the residual deformation for a plastically deformed beam does not yet match expected results.

There are still several goals that will improve the reliability, applicability, and usability of these models. While a few cantilever beam cases have been validated, extended validation will consider fixed-displacement (pinned) boundary conditions and additional load cases. Correctly modeling each case will require a more careful consideration of the appropriate way to apply various loads and enforce various boundary conditions. Further testing will also include brittle failure and plasticity in I-beams and in plates. Specifically, the hysteresis associated with plastic deformation must be reconciled.

To maximize computational efficiency, the presented results were obtained by fixing the in-plane coordinates of each node and allowing only the vertical component to vary. The presented cases are expected to exhibit almost no lateral displacements, but to generalize the model it will need to include all three degrees of freedom for each node. The code to accomplish this task was written and commented out to improve performance, so this should be a relatively easy change. The increased computational complexity may require implementation of a different solver method such

the Nonlinear Conjugate Gradient Method. Neither the bond-pair nor the bond-multiple models resist bond extension, so full degree-of-freedom models must also incorporate an extension energy term to prevent infinite transverse displacements.

A full degree-of-freedom model is necessary to extend the plate model for use with 3D thin shells. Shells are similar to plates but are not initially a flat plane. It is expected that shells can be successfully by starting with a plate and applying initial plastic deformations to all bond pairs that are not initially collinear.

By incorporating extension energy into the model, we will also gain the ability to model buckling and tension-stiffening, both of which are important to thin feature failure. Beam, plate, and shell elements should all exhibit buckling and tension stiffening behavior as a natural result of combining models that resist bending with those that resist elongation.

To make these models more useful for analysis of real parts, they should be extended to be usable with irregular discretization. For beams, this may be accomplished by using the bond-multiple model. For plates, irregular discretization might be possible using a modified bond-multiple method, or it may require the implementation of virtual points at the edges of regions with finer discretization.

Finally, the fact that the bond-pair plate model describes a material with the same Poisson ratio as a bond-pair 2D peridynamic solid suggests a means of modeling plates with arbitrary Poisson ratios. Just as the state-based linear peridynamic solid divides the deformation state into dilatory and deviatoric deformation, it may be possible to divide the bending state of a plate into spherical and deviatoric bending.

Appendix A: FRÉCHET DERIVATIVE

A.1 Definition

The derivative of a function of a state is defined by Silling in [64] as follows:

Let Ψ be a function of a state, $\Psi(\cdot) : \mathcal{A}_m \rightarrow \mathcal{L}_n$. Suppose there exists a state-valued function denoted $\nabla\Psi \in \mathcal{A}_{m+n}$ such that for any $\underline{\mathbf{A}} \in \mathcal{A}_m$ and any $\Delta\underline{\mathbf{A}} \in \mathcal{A}_m$,

$$\Psi(\underline{\mathbf{A}} + \Delta\underline{\mathbf{A}}) = \Psi(\underline{\mathbf{A}}) + \nabla\Psi(\underline{\mathbf{A}}) \bullet \Delta\underline{\mathbf{A}} + o(||\Delta\underline{\mathbf{A}}||). \quad (\text{A.1})$$

Then Ψ is said to be *differentiable* and $\nabla\Psi$ is called the *Frechet derivative* of Ψ .

This is a fairly straightforward way of defining a derivative with respect to a state. Because the force vector-state and deformation vector-state are work conjugate, the force vector-state can be determined by taking the Fréchet derivative of energy with respect to the deformation vector-state.

A.2 Bond-Pair Force

For the bond-pair model, we derive the bond force function from the bond-pair energy function

$$\begin{aligned} \underline{\mathbf{T}}\langle \xi \rangle &= \nabla w\left(\underline{\mathbf{Y}}\langle \xi \rangle\right) \\ w &= \omega(\xi) \alpha \left[1 + \cos\left(\theta\left(\underline{\mathbf{Y}}\langle \xi \rangle, \underline{\mathbf{Y}}\langle -\xi \rangle\right)\right) \right] \\ w\left(\underline{\mathbf{Y}}\langle \xi \rangle + \Delta\underline{\mathbf{Y}}\langle \xi \rangle\right) &= \omega(\xi) \alpha \left[1 + \cos\left(\theta\left(\underline{\mathbf{Y}}\langle \xi \rangle + \Delta\underline{\mathbf{Y}}\langle \xi \rangle, \underline{\mathbf{Y}}\langle -\xi \rangle\right)\right) \right] \end{aligned}$$

$$\begin{aligned} \nabla w\left(\underline{\mathbf{Y}}\langle \xi \rangle\right) \bullet \Delta\underline{\mathbf{Y}}\langle \xi \rangle &= w\left(\underline{\mathbf{Y}}\langle \xi \rangle + \Delta\underline{\mathbf{Y}}\langle \xi \rangle\right) - w\left(\underline{\mathbf{Y}}\langle \xi \rangle\right) \\ &= \omega(\xi) \alpha \sin\left(\theta\left(\underline{\mathbf{Y}}\langle \xi \rangle, \underline{\mathbf{Y}}\langle -\xi \rangle\right)\right) \left[\theta\left(\underline{\mathbf{Y}}\langle \xi \rangle + \Delta\underline{\mathbf{Y}}\langle \xi \rangle, \underline{\mathbf{Y}}\langle -\xi \rangle\right) - \theta\left(\underline{\mathbf{Y}}\langle \xi \rangle, \underline{\mathbf{Y}}\langle -\xi \rangle\right) \right] \end{aligned}$$

$$\left[\theta\left(\underline{\mathbf{Y}}\langle \xi \rangle + \Delta\underline{\mathbf{Y}}\langle \xi \rangle, \underline{\mathbf{Y}}\langle -\xi \rangle\right) - \theta\left(\underline{\mathbf{Y}}\langle \xi \rangle, \underline{\mathbf{Y}}\langle -\xi \rangle\right) \right] = \frac{\Delta\underline{\mathbf{Y}}\langle \xi \rangle}{|\underline{\mathbf{Y}}\langle \xi \rangle|} \bullet \hat{\theta}\left(\underline{\mathbf{Y}}\langle \xi \rangle, \underline{\mathbf{Y}}\langle -\xi \rangle\right)$$

To determine the $\hat{\theta}$ direction vector, we must construct a vector that is normal to $\underline{Y}\langle\xi\rangle$ and that is in the plane containing both $\underline{Y}\langle\xi\rangle$ and $\underline{Y}\langle-\xi\rangle$. The cross product of $\underline{Y}\langle\xi\rangle$ and $\underline{Y}\langle-\xi\rangle$ is a vector normal to that plane, so any vector normal to that cross product will be in the correct plane. Therefore, the vector $\underline{Y}\langle\xi\rangle \times [\underline{Y}\langle\xi\rangle \times \underline{Y}\langle-\xi\rangle]$ is both normal to $\underline{Y}\langle\xi\rangle$ and is in the plane containing both $\underline{Y}\langle\xi\rangle$ and $\underline{Y}\langle-\xi\rangle$. Normalizing gives us the $\hat{\theta}$ direction vector:

$$\hat{\theta}(\underline{Y}\langle\xi\rangle, \underline{Y}\langle-\xi\rangle) = \frac{\underline{Y}\langle\xi\rangle \times [\underline{Y}\langle\xi\rangle \times \underline{Y}\langle-\xi\rangle]}{|\underline{Y}\langle\xi\rangle||\underline{Y}\langle\xi\rangle||\underline{Y}\langle-\xi\rangle| \sin(\theta(\underline{Y}\langle\xi\rangle, \underline{Y}\langle-\xi\rangle))}$$

We combine all of these to get the expression for bond force found in eq. (5.1).

$$\underline{T}\langle\xi\rangle = \omega(\xi) \frac{-\alpha}{|\underline{Y}\langle\xi\rangle|} \frac{\underline{Y}\langle\xi\rangle}{|\underline{Y}\langle\xi\rangle|} \times \left[\frac{\underline{Y}\langle\xi\rangle}{|\underline{Y}\langle\xi\rangle|} \times \frac{\underline{Y}\langle-\xi\rangle}{|\underline{Y}\langle-\xi\rangle|} \right]$$

A.3 Isotropic Bending Correction

To derive the bending “pressure” force, we start with the isotropic energy discrepancy

$$W' = 2G \frac{h^3}{12} \frac{3\nu - 1}{1 - \nu} \bar{\kappa}^2.$$

with

$$\begin{aligned} \bar{\kappa}(\underline{Y}) &= \frac{1}{m} \int_0^\delta \int_0^{2\pi} \omega(\xi) \frac{\underline{Y}\langle\xi\rangle + \underline{Y}\langle-\xi\rangle}{\xi^2} \xi d\phi d\xi \\ &= \frac{2}{m} \int_0^\delta \int_0^{2\pi} \omega(\xi) \frac{\underline{Y}\langle\xi\rangle}{\xi^2} \xi d\phi d\xi \end{aligned}$$

Because $\bar{\kappa}$ is itself a vector-state, we will need to begin with the change in $\bar{\kappa}$ with respect to \underline{Y} and carry the result through to find the change in W' .

$$\begin{aligned}\bar{\kappa}(\underline{Y} + \Delta\underline{Y}) &= \frac{2}{m} \int_0^\delta \int_0^{2\pi} \omega(\xi) \frac{\underline{Y}\langle\xi\rangle + \Delta\underline{Y}\langle\xi\rangle}{\xi^2} \xi d\phi d\xi \\ &= \bar{\kappa}(\underline{Y}) + \frac{2}{m} \int_0^\delta \int_0^{2\pi} \omega(\xi) \frac{\Delta\underline{Y}\langle\xi\rangle}{\xi^2} \xi d\phi d\xi\end{aligned}$$

$$\begin{aligned}W'(\underline{Y} + \Delta\underline{Y}) &= 2G \frac{h^3}{12} \frac{3\nu - 1}{1 - \nu} [\bar{\kappa}(\underline{Y} + \Delta\underline{Y})]^2 \\ &= 2G \frac{h^3}{12} \frac{3\nu - 1}{1 - \nu} \left\{ \bar{\kappa}(\underline{Y}) \cdot \bar{\kappa}(\underline{Y}) \right. \\ &\quad + \frac{4}{m} \int_0^\delta \int_0^{2\pi} \omega(\xi) \frac{\Delta\underline{Y}\langle\xi\rangle \cdot \bar{\kappa}(\underline{Y})}{\xi^2} \xi d\phi d\xi \\ &\quad \left. + \frac{2}{m} \int_0^\delta \int_0^{2\pi} \omega(\xi) \frac{\Delta\underline{Y}\langle\xi\rangle \cdot \Delta\underline{Y}\langle\xi\rangle}{\xi^2} \xi d\phi d\xi \right\} \\ &= W'(\underline{Y}) + 2G \frac{h^3}{12} \frac{3\nu - 1}{1 - \nu} \frac{4}{m} \frac{\omega(\xi)}{\xi^2} \bar{\kappa}(\underline{Y}) \bullet \Delta\underline{Y} + o(||\Delta\underline{Y}||) \\ \nabla W'(\underline{Y}) &= \underline{T}\langle\xi\rangle = \frac{8G}{m} \frac{h^3}{12} \frac{3\nu - 1}{1 - \nu} \frac{\omega(\xi)}{\xi^2} \bar{\kappa}\end{aligned}$$

This demonstrates the bond-length dependent “pressure” applied to each point in the neighborhood of a point with average curvature $\bar{\kappa}$.

Appendix B: NOTATIONS

Here we show the use of multiple appendixes.

B.1 Math Notations

Each appendix can have sub-sections as a regular chapter.

BIBLIOGRAPHY

- [1] R Ansari, S Sahmani, and B Arash. Nonlocal plate model for free vibrations of single-layered graphene sheets. *Physics Letters A*, 375(1):53–62, 2010.
- [2] Douglas N Arnold. An interior penalty finite element method with discontinuous elements. *SIAM journal on numerical analysis*, 19(4):742–760, 1982.
- [3] E. Askari, F. Bobaru, RB Lehoucq, ML Parks, SA Silling, and O. Weckner. Peridynamics for multiscale materials modeling. In *Journal of Physics: Conference Series*, volume 125, page 012078. IOP Publishing, 2008.
- [4] Zdenek P Bazant and Ta-Peng Chang. Nonlocal finite element analysis of strain-softening solids. *Journal of engineering mechanics*, 113(1):89–105, 1987.
- [5] Zdenek P Bazant and Gilles Pijaudier-Cabot. Nonlocal continuum damage, localization instability and convergence. *Journal of Applied Mechanics*, 55(2):287–293, 1988.
- [6] Ted Belytschko and Tom Black. Elastic crack growth in finite elements with minimal remeshing. *International journal for numerical methods in engineering*, 45(5):601–620, 1999.
- [7] W Benz and E Asphaug. Simulations of brittle solids using smooth particle hydrodynamics. *Computer physics communications*, 87(1):253–265, 1995.
- [8] Florin Bobaru. Influence of van der waals forces on increasing the strength and toughness in dynamic fracture of nanofibre networks: a peridynamic approach. *Modelling and Simulation in Materials Science and Engineering*, 15(5):397, 2007.
- [9] Florin Bobaru and Monchai Duangpanya. The peridynamic formulation for transient heat conduction. *International Journal of Heat and Mass Transfer*, 53(19):4047–4059, 2010.

- [10] Nathaniel Burch and Richard Lehoucq. Classical, nonlocal, and fractional diffusion equations on bounded domains. *International Journal for Multiscale Computational Engineering*, 9(6), 2011.
- [11] J Burghardt, R Brannon, and J Guilkey. A nonlocal plasticity formulation for the material point method. *Computer Methods in Applied Mechanics and Engineering*, 225:55–64, 2012.
- [12] N Challamel and C M Wang. The small length scale effect for a non-local cantilever beam: a paradox solved. *Nanotechnology*, 19(34):345703, 2008.
- [13] RJ Cheng and Kim Meow Liew. Analyzing two-dimensional sine–gordon equation with the mesh-free reproducing kernel particle ritz method. *Computer methods in applied mechanics and engineering*, 245:132–143, 2012.
- [14] Gianluca Cusatis, Andrea Mencarelli, Daniele Pelessone, and James Baylot. Lattice discrete particle model (ldpm) for failure behavior of concrete. ii: Calibration and validation. *Cement and Concrete Composites*, 33(9):891–905, 2011.
- [15] Gianluca Cusatis, Daniele Pelessone, and Andrea Mencarelli. Lattice discrete particle model (ldpm) for failure behavior of concrete. i: Theory. *Cement and Concrete Composites*, 33(9):881–890, 2011.
- [16] Kaushik Dayal and Kaushik Bhattacharya. Kinetics of phase transformations in the peridynamic formulation of continuum mechanics. *Journal of the Mechanics and Physics of Solids*, 54(9):1811–1842, 2006.
- [17] Paul N Demmie and Stewart A Silling. An approach to modeling extreme loading of structures using peridynamics. *Journal of Mechanics of Materials and Structures*, 2(10):1921–1945, 2007.

- [18] John Dolbow, Nicolas Moës, and Ted Belytschko. Modeling fracture in mindlin–reissner plates with the extended finite element method. *International Journal of Solids and Structures*, 37(48):7161–7183, 2000.
- [19] WH Duan and CM Wang. Exact solutions for axisymmetric bending of micro/nanoscale circular plates based on nonlocal plate theory. *Nanotechnology*, 18(38):385704, 2007.
- [20] Etienne Emmrich and Olaf Weckner. Analysis and numerical approximation of an integro-differential equation modeling non-local effects in linear elasticity. *Mathematics and Mechanics of Solids*, 12(4):363–384, 2007.
- [21] A Cemal Eringen. On differential equations of nonlocal elasticity and solutions of screw dislocation and surface waves. *Journal of Applied Physics*, 54(9):4703–4710, 1983.
- [22] A.C. Eringen and DGB Edelen. On nonlocal elasticity. *International Journal of Engineering Science*, 10(3):233–248, 1972.
- [23] XJ Fang, QD Yang, BN Cox, and ZQ Zhou. An augmented cohesive zone element for arbitrary crack coalescence and bifurcation in heterogeneous materials. *International Journal for Numerical Methods in Engineering*, 88(9):841–861, 2011.
- [24] Thomas M Fischer. Bending stiffness of lipid bilayers. iii. gaussian curvature. *Journal de Physique II*, 2(3):337–343, 1992.
- [25] John Foster, Stewart A. Silling, and Weinong Chen. An energy based failure criterion for use with peridynamic states. *International Journal for Multiscale Computational Engineering*, 9(6):675–988, 2011.
- [26] JT Foster, SA Silling, and WW Chen. Viscoplasticity using peridynamics. *International Journal for Numerical Methods in Engineering*, 81(10):1242–1258, 2010.

- [27] JW Foulk, DH Allen, and KLE Helms. Formulation of a three-dimensional cohesive zone model for application to a finite element algorithm. *Computer methods in applied mechanics and engineering*, 183(1):51–66, 2000.
- [28] Thomas-Peter Fries and Ted Belytschko. The extended/generalized finite element method: an overview of the method and its applications. *International Journal for Numerical Methods in Engineering*, 84(3):253–304, 2010.
- [29] Walter Gerstle, Nicolas Sau, and Stewart Silling. Peridynamic modeling of concrete structures. *Nuclear engineering and design*, 237(12):1250–1258, 2007.
- [30] PC Guan, JS Chen, Y Wu, H Teng, J Gaidos, K Hofstetter, and M Alsaleh. Semi-lagrangian reproducing kernel formulation and application to modeling earth moving operations. *Mechanics of Materials*, 41(6):670–683, 2009.
- [31] PC Guan, SW Chi, JS Chen, TR Slawson, and MJ Roth. Semi-lagrangian reproducing kernel particle method for fragment-impact problems. *International Journal of Impact Engineering*, 38(12):1033–1047, 2011.
- [32] M Holl, S Loehnert, and P Wriggers. An adaptive multiscale method for crack propagation and crack coalescence. *International Journal for Numerical Methods in Engineering*, 93(1):23–51, 2013.
- [33] Michael J Hunsweck, Yongxing Shen, and Adrián J Lew. A finite element approach to the simulation of hydraulic fractures with lag. *International Journal for Numerical and Analytical Methods in Geomechanics*, 37(9):993–1015, 2013.
- [34] B. Kilic, A. Agwai, and E. Madenci. Peridynamic theory for progressive damage prediction in center-cracked composite laminates. *Composite Structures*, 90(2):141–151, 2009.
- [35] Bahattin Kilic and Erdogan Madenci. Prediction of crack paths in a quenched glass plate by using peridynamic theory. *International journal of fracture*, 156(2):165–177, 2009.

- [36] E. Kröner. Elasticity theory of materials with long range cohesive forces. *International Journal of Solids and Structures*, 3(5):731–742, 1967.
- [37] Shaofan Li, Wei Hao, and Wing Kam Liu. Numerical simulations of large deformation of thin shell structures using meshfree methods. *Computational Mechanics*, 25(2-3):102–116, 2000.
- [38] Weizhou Li and Thomas Siegmund. An analysis of crack growth in thin-sheet metal via a cohesive zone model. *Engineering Fracture Mechanics*, 69(18):2073–2093, 2002.
- [39] David John Littlewood. Simulation of dynamic fracture using peridynamics, finite element modeling, and contact. Technical report, Sandia National Laboratories, 2010.
- [40] Wing Kam Liu, Sukky Jun, and Yi Fei Zhang. Reproducing kernel particle methods. *International journal for numerical methods in fluids*, 20(8-9):1081–1106, 1995.
- [41] Éamonn Ó Máirtín, Guillaume Parry, Glenn E Beltz, and J Patrick McGarry. Potential-based and non-potential-based cohesive zone formulations under mixed-mode separation and overclosure—part ii: Finite element applications. *Journal of the Mechanics and Physics of Solids*, 63:363–385, 2014.
- [42] Bertrand Maurel and Alain Combescure. An sph shell formulation for plasticity and fracture analysis in explicit dynamics. *International journal for numerical methods in engineering*, 76(7):949–971, 2008.
- [43] J Patrick McGarry, Éamonn Ó Máirtín, Guillaume Parry, and Glenn E Beltz. Potential-based and non-potential-based cohesive zone formulations under mixed-mode separation and overclosure. part i: Theoretical analysis. *Journal of the Mechanics and Physics of Solids*, 63:336–362, 2014.

- [44] Jens Markus Melenk and Ivo Babuska. The partition of unity finite element method: basic theory and applications. *Computer methods in applied mechanics and engineering*, 139(1):289–314, 1996.
- [45] M Memar Ardestani, B Soltani, and Sh Shams. Analysis of functionally graded stiffened plates based on fsdt utilizing reproducing kernel particle method. *Composite Structures*, 112:231–240, 2014.
- [46] Y. Mikata. Analytical solutions of peristatic and peridynamic problems for a 1d infinite rod. *International Journal of Solids and Structures*, 2012.
- [47] J.A. Mitchell. A nonlocal, ordinary, state-based plasticity model for peridynamics. Technical report, Sandia National Laboratories, 2011.
- [48] John A Mitchell. A non-local, ordinary-state-based viscoelasticity model for peridynamics. Technical report, Tech. Report SAND2011-8064, Sandia National Laboratories, 2011.
- [49] Nicolas Moes, John Dolbow, and T Belytschko. A finite element method for crack growth without remeshing. *Int. J. Numer. Meth. Engng*, 46:131–150, 1999.
- [50] T Mohammadnejad and AR Khoei. Hydro-mechanical modeling of cohesive crack propagation in multiphase porous media using the extended finite element method. *International Journal for Numerical and Analytical Methods in Geomechanics*, 37(10):1247–1279, 2013.
- [51] Joe J Monaghan. Smoothed particle hydrodynamics. *Reports on progress in physics*, 68(8):1703, 2005.
- [52] John A Nairn. Material point method calculations with explicit cracks. *Computer Modeling in Engineering and Sciences*, 4(6):649–664, 2003.
- [53] A Needleman. A continuum model for void nucleation by inclusion debonding. *Journal of applied mechanics*, 54(3):525–531, 1987.

- [54] James O’Grady and John T Foster. Peridynamic beams: A non-ordinary, state-based model. *International Journal of Solids and Structures*, 51(18):3177–3183, September 2014.
- [55] Michael Ortiz, Yves Leroy, and Alan Needleman. A finite element method for localized failure analysis. *Computer Methods in Applied Mechanics and Engineering*, 61(2):189–214, 1987.
- [56] Mario Di Paola, Giuseppe Failla, and Massimiliano Zingales. Mechanically based nonlocal euler-bernoulli beam model. *Journal of Nanomechanics and Micromechanics*, 4(1), 2014.
- [57] SC Pradhan and T Murmu. Small scale effect on the buckling of single-layered graphene sheets under biaxial compression via nonlocal continuum mechanics. *Computational Materials Science*, 47(1):268–274, 2009.
- [58] Junuthula Narasimha Reddy. *Theory and analysis of elastic plates and shells*. CRC press, 2007.
- [59] A. Sadeghirad, R. M. Brannon, and J. Burghardt. A convected particle domain interpolation technique to extend applicability of the material point method for problems involving massive deformations. *International Journal for Numerical Methods in Engineering*, 86(12):1435–1456, 2011.
- [60] Henning Sauerland and Thomas-Peter Fries. The stable xfem for two-phase flows. *Computers & Fluids*, 87:41–49, 2013.
- [61] A Shyam and E Lara-Curzio. The double-torsion testing technique for determination of fracture toughness and slow crack growth behavior of materials: a review. *Journal of materials science*, 41(13):4093–4104, 2006.
- [62] S.A. Silling. Reformulation of elasticity theory for discontinuities and long-range forces. *Journal of the Mechanics and Physics of Solids*, 48(1):175–209, 2000.

- [63] S.A. Silling. A coarsening method for linear peridynamics. *International Journal for Multi-scale Computational Engineering*, 9(6):609, 2011.
- [64] SA Silling, M. Epton, O. Weckner, J. Xu, and E. Askari. Peridynamic states and constitutive modeling. *Journal of Elasticity*, 88(2):151–184, 2007.
- [65] SA Silling and RB Lehoucq. Peridynamic theory of solid mechanics. *Advances in Applied Mechanics*, 44:73–168, 2010.
- [66] Stewart A Silling and Ebrahim Askari. A meshfree method based on the peridynamic model of solid mechanics. *Computers & Structures*, 83(17):1526–1535, 2005.
- [67] STEWART A Silling, M Zimmermann, and R Abeyaratne. Deformation of a peridynamic bar. *Journal of Elasticity*, 73(1-3):173–190, 2003.
- [68] Stewart Andrew Silling and Florin Bobaru. Peridynamic modeling of membranes and fibers. *International Journal of Non-Linear Mechanics*, 40(2):395–409, 2005.
- [69] Volker Springel. Smoothed particle hydrodynamics in astrophysics. *Annual Review of Astronomy and Astrophysics*, 48:391–430, 2010.
- [70] Deborah Sulsky and Howard L Schreyer. Axisymmetric form of the material point method with applications to upsetting and taylor impact problems. *Computer Methods in Applied Mechanics and Engineering*, 139(1):409–429, 1996.
- [71] Michael Taylor and David J Steigmann. A two-dimensional peridynamic model for thin plates. *Mathematics and Mechanics of Solids*, 2013.
- [72] Stephen Timoshenko, Sergius Woinowsky-Krieger, and S Woinowsky. *Theory of plates and shells*, volume 2. McGraw-hill New York, 1959.
- [73] MR Tupek, JJ Rimoli, and R Radovitzky. An approach for incorporating classical continuum damage models in state-based peridynamics. *Computer Methods in Applied Mechanics and Engineering*, 2013.

- [74] R Vignjevic, N Djordjevic, S Gemkow, T De Vuyst, and J Campbell. Sph as a nonlocal regularisation method: Solution for instabilities due to strain-softening. *Computer Methods in Applied Mechanics and Engineering*, 277:281–304, 2014.
- [75] T.L. Warren, S.A. Silling, A. Askari, O. Weckner, M.A. Epton, and J. Xu. A non-ordinary state-based peridynamic method to model solid material deformation and fracture. *International Journal of Solids and Structures*, 46(5):1186–1195, 2009.
- [76] O. Weckner and R. Abeyaratne. The effect of long-range forces on the dynamics of a bar. *Journal of the Mechanics and Physics of Solids*, 53(3):705–728, 2005.
- [77] O. Weckner, G. Brunk, M.A. Epton, S.A. Silling, and E. Askari. Green’s functions in non-local three-dimensional linear elasticity. *Proceedings of the Royal Society A: Mathematical, Physical and Engineering Science*, 465(2111):3463–3487, 2009.
- [78] Z Wieckowski. The material point method in large strain engineering problems. *Computer methods in applied mechanics and engineering*, 193(39):4417–4438, 2004.
- [79] Youcai Wu, Joseph M Magallanes, and John E Crawford. Fragmentation and debris evolution modeled by a point-wise coupled reproducing kernel/finite element formulation. *International Journal of Damage Mechanics*, page 1056789514520797, 2014.
- [80] Yongning Xie and Gang Wang. A stabilized iterative scheme for coupled hydro-mechanical systems using reproducing kernel particle method. *International Journal for Numerical Methods in Engineering*, 2014.
- [81] J. Xu, A. Askari, O. Weckner, and S. Silling. Peridynamic analysis of impact damage in composite laminates. *Journal of Aerospace Engineering*, 21:187, 2008.
- [82] Jin Xu, Chi King Lee, and KH Tan. An xfem plate element for high gradient zones resulted from yield lines. *International Journal for Numerical Methods in Engineering*, 93(12):1314–1344, 2013.

VITA

This should be a one-page short vita.

There can be more paragraphs.